nature cardiovascular research

Article

https://doi.org/10.1038/s44161-025-00691-5

Inhibition of proprotein convertase SKI-1 prevents blood vessel alteration after stroke

Received: 24 April 2024

Accepted: 16 July 2025

Alireza P. Shabanzadeh[1,2,3], Dene Ringuette[1,3,4], Michal Syonov[1,3,4], Qisi Wu[5], Nardos G. Tassew[1], Eric K. Mun[1,3,4], Autumn Meek[1], Starlee Lively[1], Samuel E. Suntharalingham[1,4], Mia Mojica[6], Leonardo Olijnyk[1], Beiping Qiang[7], Warren D. Foltz[8], Mark Reed[1,9], Ignace Moya[1], Carla Brown[1], Jinzhou Feng[5], Xinyue Qin[5], Pavan Sudheer Akula[1], Thomas Wälchli[1,2,10,11], Peter L. Carlen[1,2,4], Paula Alcaide-Leon[12] & Philippe P. Monnier[1,2,3,4,13] ✉

Neutralizing factors involved in blood vessel dysfunction offer a promising strategy for stroke recovery. Many extracellular proteins need enzymatic activation to function, and blocking this activation is an untapped approach to restoring vessel integrity. Here we demonstrate that inhibition of the extracellular protease SKI-1 with PF-429242 restores blood vessel integrity and promotes functional recovery in both large and small animal models for stroke. Single-cell mRNA sequencing identified molecular signatures suggesting that PF-429242 restores the expression of genes involved in vessel integrity in endothelial cells. Moreover, we identify a mechanism whereby RGMa cleavage by SKI-1 is required for RGMa to interact with Neogenin and alter vessel integrity. Either preventing RGMa cleavage or deleting Neogenin on endothelial cells reduced blood vessel dysfunction, increased tissue preservation and restored brain function after stroke. This work identifies a much-needed therapeutic strategy that restores blood vessel integrity and functionality, showing efficacy in large and small animals.

The central nervous system (CNS) is protected from harmful blood-borne factors by endothelial cells of the blood–brain barrier (BBB). Ischemic stroke triggers blood vessel alterations and BBB leakiness that tightly correlate with ensuing brain damage and loss of function. Preventing BBB dysfunction after stroke may protect brain cells and represents an attractive potential treatment to maintain adequate brain function[1–3].

Extracellular proteins play key roles in stroke-related cellular events[3], influencing neuronal survival and regeneration. Recent studies suggest that targeting extracellular proteins may help restore blood vessel integrity after stroke. For instance, engineered Wnt ligands[3] and RGMa silencing via adeno-associated virus (AAV)-short hairpin RNA (shRNA) delivery both improved blood vessel integrity in stroke models[4].

Many extracellular proteins require enzymatic activation to function[5]. Thus, blocking their activation could help prevent stroke-induced vascular damage. Proprotein convertases (PPCs)—a family of secreted enzymes—activate various extracellular proteins and are implicated in inflammation, viral infection, cancer, Alzheimer's disease and hypercholesterolemia[6,7]. PPCs are appealing drug targets; for example, PCSK9 inhibitors are now used to lower cholesterol[8]. However, the role of PPCs in diseases such as stroke, multiple sclerosis or Alzheimer's is still largely unexplored.

Subtilisin kexin isozyme-1 (SKI-1) is one of the least-studied PPCs. In development, SKI-1 activates the cell surface ligand RGMa thereby contributing to axon guidance[9]. Although RGMa contributes to stroke[10] and multiple sclerosis pathology[11], the role of SKI-1 in these conditions is unknown. The discovery of PF-429242, a selective SKI-1 inhibitor, enables investigation of its function in disease. SKI-1 has primarily been studied for its antiviral effects, including inhibiting Lassa virus and hepatitis C virus[12], and for anticancer properties in glioblastoma and liver cancer cells[13]. Whether SKI-1 affects vascular integrity in stroke or other CNS diseases remains unclear.

A full list of affiliations appears at the end of the paper. ✉e-mail: pmonnier@uhnres.utoronto.ca

In the present study, we assessed the role of SKI-1 inhibition on vascular integrity after ischemic stroke in large and small animal models. Single-cell RNA sequencing (scRNA-seq) revealed that PF-429242 alters the expression of several genes regulating vascular function. We also found that SKI-1-mediated RGMa processing is necessary for RGMa to interact with Neogenin and disrupt blood vessels after stroke.

Results

PF-429242 restores genes involved in blood vessel integrity

SKI-1 knockout mice are embryonic lethal, but the small-molecule SKI-1 inhibitor PF-429242 allows investigation of the role of SKI-1 in blood vessel integrity after stroke. We hypothesized that PF-429242 might prevent stroke-induced vascular changes by gene expression in endothelial cells. To test this, we performed scRNA-seq[14] on endothelial cells ($CD31^+/CD45^-$) isolated via fluorescence-activated cell sorting (FACS) from brains of C57BL/6J mice subjected to middle cerebral artery occlusion (MCAO) and treated with PF-429242 or vehicle (Fig. 1a and Extended Data Fig. 1a–d). Three days after MCAO, endothelial cells expressing *Pecam1*/CD31 and *Cdh5* (cadherin 5) were analyzed (Fig. 1b).

Three endothelial-cell-specific gene signatures were depleted in the ipsilateral MCAO hemisphere relative to the contralateral hemisphere and sham MCAO procedures for which PF-429242 treatment ablated the depletion (Fig. 1c). One key signature included *Ntn4* (netrin 4), *Fbln2* (nibulin 2) and *Cdh13* (cadherin 13) genes involved in vascular stability and endothelial survival[15–17], suggesting that SKI-1 inhibition may preserve vascular integrity. Two other downregulated signatures involved ribosomal, transcriptional and antiviral genes including *Cfh*, a regulator of BBB permeability and a known suppressor of a pathway implicated in increasing BBB permeability and a factor in macular degeneration[18]. Notably, *Ntn4* was more associated with large artery and *Cfh* with veins (Fig. 1d).

A separate endothelial-cell-specific gene set was upregulated in the ipsilateral hemisphere but suppressed by PF-429242 (Fig. 1e,f). This set included both pro-leakage genes such as *Bsg* (basigin/CD147 (ref. 19)) and *Cxcl12*/SDF-1 (ref. 20) and protective genes such as *Igf1r*, *Id1*, *Jcad* and *Spock2*. *Cldn5* was upregulated in the ipsilateral untreated MCAO hemisphere, possibly as a compensatory mechanism. The depletion of this enriched gene signature due to PF-429242 treatment occurs predominately in the middle capillaries, with the gene signature being retained in only a small cluster of arterial and venule capillary subtypes (Fig. 1f,g). Notably, half of the endothelial cells in the *Cfh* signature also expressed *Il1r1* and did not overlap with *Cxcl12*-expressing endothelial cells, suggesting the presence of endothelial cell subtypes.

Total endothelial cell transcript differences are shown in Fig. 2a,b. PF-429242 treatment significantly reduced expression of *Bsg* and three solute carrier genes (*Slc39a10*, *Slco1a4* and *Slco1c1*). Differences between hemispheres were less pronounced than those between treatment groups, suggesting that both stroke and treatment effects are partly bilateral. Fold changes for key signature genes and similarly varying transcripts are shown in Fig. 2c, along with selected expression profiles.

PF-429242 reversed MCAO-induced increases in *Cxcl12*, *Car4* (carbonic anhydrase 4)[21] and *Bsg*. Immunostaining confirmed these changes, showing higher protein levels around endothelial cells in vehicle-treated brains compared to PF-429242-treated tissue in the ipsilateral MCAO region (Fig. 2d–f). These results suggest that SKI-1 inhibition by PF-429242 restores gene expression linked to vascular integrity after stroke.

PF-429242 restores BBB integrity and behaviors

Having shown that PF-429242 affects genes involved in vascular function, we tested whether it also restores blood vessel integrity after MCAO. Mice received 30 mg kg^{-1} PF-429242 via intraperitoneal injection immediately after MCAO (Fig. 3). Laser Doppler flowmetry (LDF) confirmed equivalent reperfusion in both PF-429242-treated and vehicle-treated wild-type (WT) mice (Extended Data Fig. 2a–c).

Two days after MCAO, Texas Red dextran (TR-dextran) was injected intravenously, and mice were perfused to clear residual dye. Lightsheet imaging of iDISCO-cleared brains showed strong TR-dextran accumulation in the right hemisphere of MCAO control mice, indicating leakage (Fig. 3a). PF-429242 treatment significantly reduced TR-dextran extravasation compared to controls ($P = 0.035$).

To test effects beyond the brain, we induced retinal ischemia in rats via ophthalmic artery ligation. Evans blue dye analysis showed significantly reduced blood–retinal barrier (BRB) leakage in PF-429242-treated rats (Extended Data Fig. 3a). In contrast, liver ischemia-induced vascular leak was not affected by PF-429242 (Extended Data Fig. 3b).

These results suggest that SKI-1 is required for ischemia-induced vascular leakage in the CNS and that its inhibition preserves vessel integrity after stroke in brain and retina.

Pericytes are crucial for maintaining BBB integrity, and preserving pericyte coverage supports recovery after stroke[22]. Restoration of the BBB can prevent immune cell infiltration, which contributes to post-stroke damage[23]. We examined immune cell presence in the MCAO penumbra using CD68 (macrophage marker)[24] and CD45 (hematopoietic cells)[25]. PF-429242 reduced $CD45^+$ and $CD68^+$ cells by 69.4 ± 5.8% ($P < 0.0001$) and 62.9 ± 7.6% ($P = 0.005$), respectively (Extended Data Fig. 4a; percentage confidence intervals correspond to error propagated mean ± s.e.m. intervals of compared samples). Although a direct effect on immune cells cannot be ruled out, this reduction supports a role in BBB preservation.

To assess neuronal protection, we quantified $NeuN^+$ neurons in the peri-infarct region. PF-429242 increased neuron numbers by 110.9 ± 34.4% ($P = 0.0003$; Fig. 3c). This was due to reduced neuronal death, as Fluoro-Jade C (FJC) staining showed a 57.2 ± 8.7% decrease in degenerating neurons ($P = 0.001$; Fig. 3d).

We then assessed axonal preservation using neurofilament heavy chain (NEFH) staining. PF-429242 increased $NEFH^+$ cells by 89.4 ± 25.5% ($P = 0.002$; Fig. 3e), indicating improved axonal network integrity in the injured hemisphere.

To examine apoptosis, we performed anti-caspase-3 staining. PF-429242 significantly increased overall cell survival. However, co-staining with IB4 revealed that endothelial cell death was unaffected, indicating that the drug does not prevent endothelial apoptosis (Extended Data Fig. 4b).

BBB restoration prevents toxic blood components from leaking, reducing astroglial activation after stroke. PF-429242 treatment decreased $GFAP^+$ astrocyte activation by 66.7 ± 12.2% ($P = 0.027$) compared to controls (Fig. 3f). Overall, inhibiting SKI-1 with PF-429242 reduced astrocyte reactivity while preserving neurons and axons.

Staining with 2,3,5-triphenyltetrazolium chloride (TTC) showed that PF-429242 significantly reduced infarct volume by 73.5 ± 6.2% ($P = 0.0003$) and edema size by 51.3 ± 16.2% ($P = 0.036$) compared to controls (Extended Data Fig. 3c–e). Lower brain water content confirmed reduced edema (Extended Data Fig. 3f).

Neurobehavioral tests assessing sensorimotor and cognitive function were performed before and up to 7 days after MCAO. Vital signs and body weight loss were similar between groups (Extended Data Figs. 5 and 6a). PF-429242 treatment significantly improved locomotion, asymmetry and Neurological Severity Scores (NSSs) (Fig. 3g–i). The open field test showed an 86.7 ± 14.5% increase in distance traveled and an 87.3 ± 9.4% increase in activity versus controls (Fig. 3g and Extended Data Fig. 6b). Functional recovery was also evident in Bederson scores and modified NSSs (Fig. 3h,j)[10].

Finally, seizure activity measured by the Racine scale[10] was significantly reduced in PF-429242 mice during the first 3 days after MCAO (Fig. 3k). By day 3, treated mice showed no seizures, whereas controls still exhibited seizure activity.

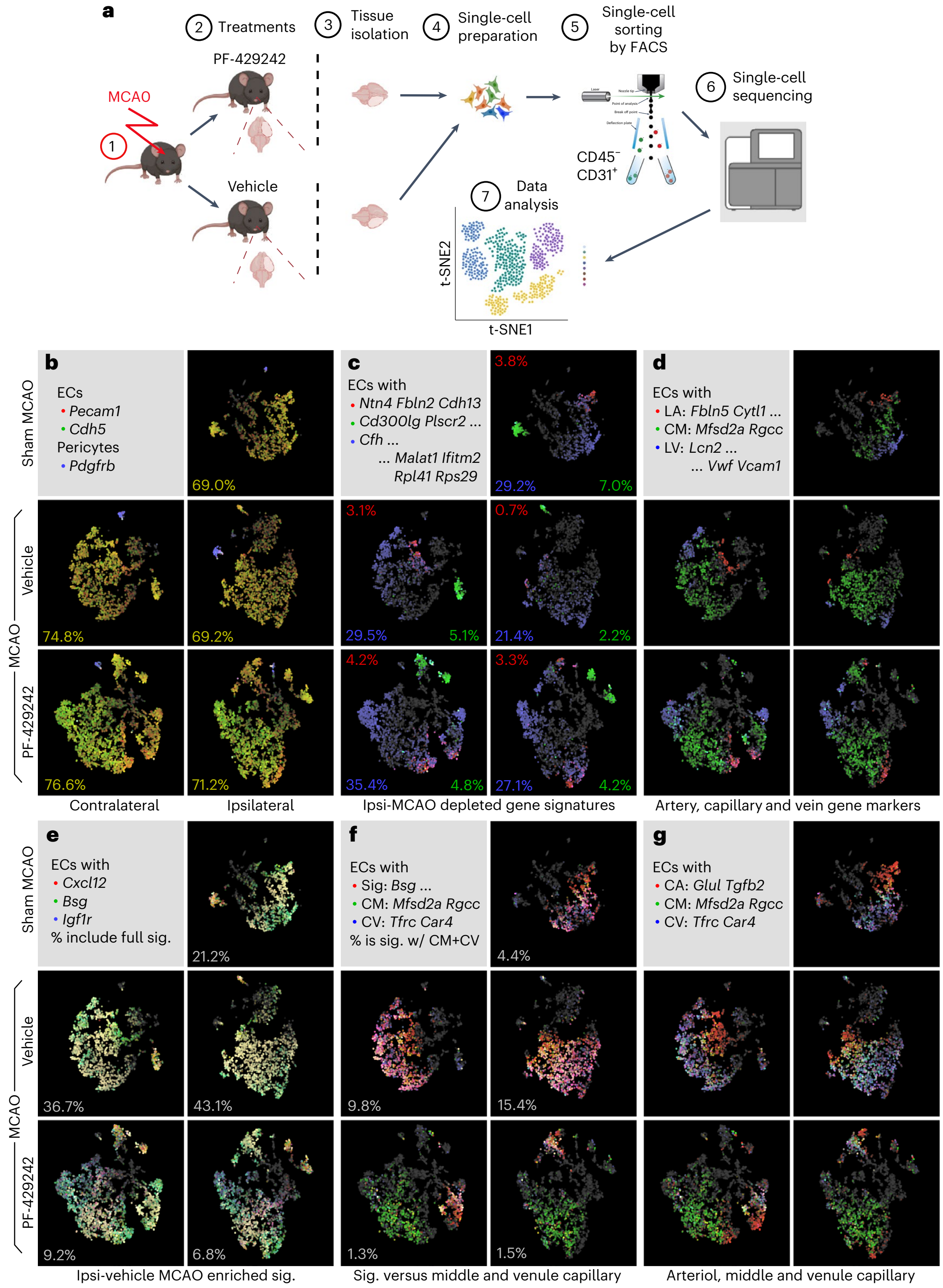

Fig. 1 | Gene expression signatures associated with PF-429242 rescue. **a**, Schematic of the protocol used to study the role of SKI-1 in stroke: mice received MCAO followed by treatment with PF-429242 or PBS. Two days after MCAO, brains were collected and dissociated into single cells; endothelial cells were isolated using FACS; and mRNA sequencing of single cells was performed and analyzed (https://biorender.com/ytb0wjd). **b**–**g**, Expression overlaid t-SNE plots of gene markers (intensity indicates mean $\log_2$ expression of each marker) and signatures (intensity corresponds to geometric mean of expression of genes in the signature) across five conditions: sham MCAO (right hemisphere), untreated MCAO (separate left and right hemispheres) and PF-429242-treated MCAO (also separate hemispheres). **b**, Common EC and pericyte markers in $CD31^+$ cells isolated through FACS. **c**, Three related gene signatures depleted in the ipsilateral untreated MCAO condition. **d**, Gene signatures for large arteries (LA) and veins (LV) versus middle capillaries (CM) indicating that two depleted signatures share similarity with large vessel ECs, and one depleted signature lacks association with vessel-type-specific markers. Inset percentages correspond to the fraction of cells showing signature expression. **e**, Ipsilateral untreated MCAO enriched genes associated with a signature enriched in the ipsilateral untreated MCAO condition. **f**, Enriched gene signature verses middle and venule capillary (CV) gene signatures. **g**, Arterial (CA), middle and venule capillary signatures indicating that depletion of the enriched signature due to PF-429242 rescue occurs predominately in the middle capillaries. EC, endothelial cell.

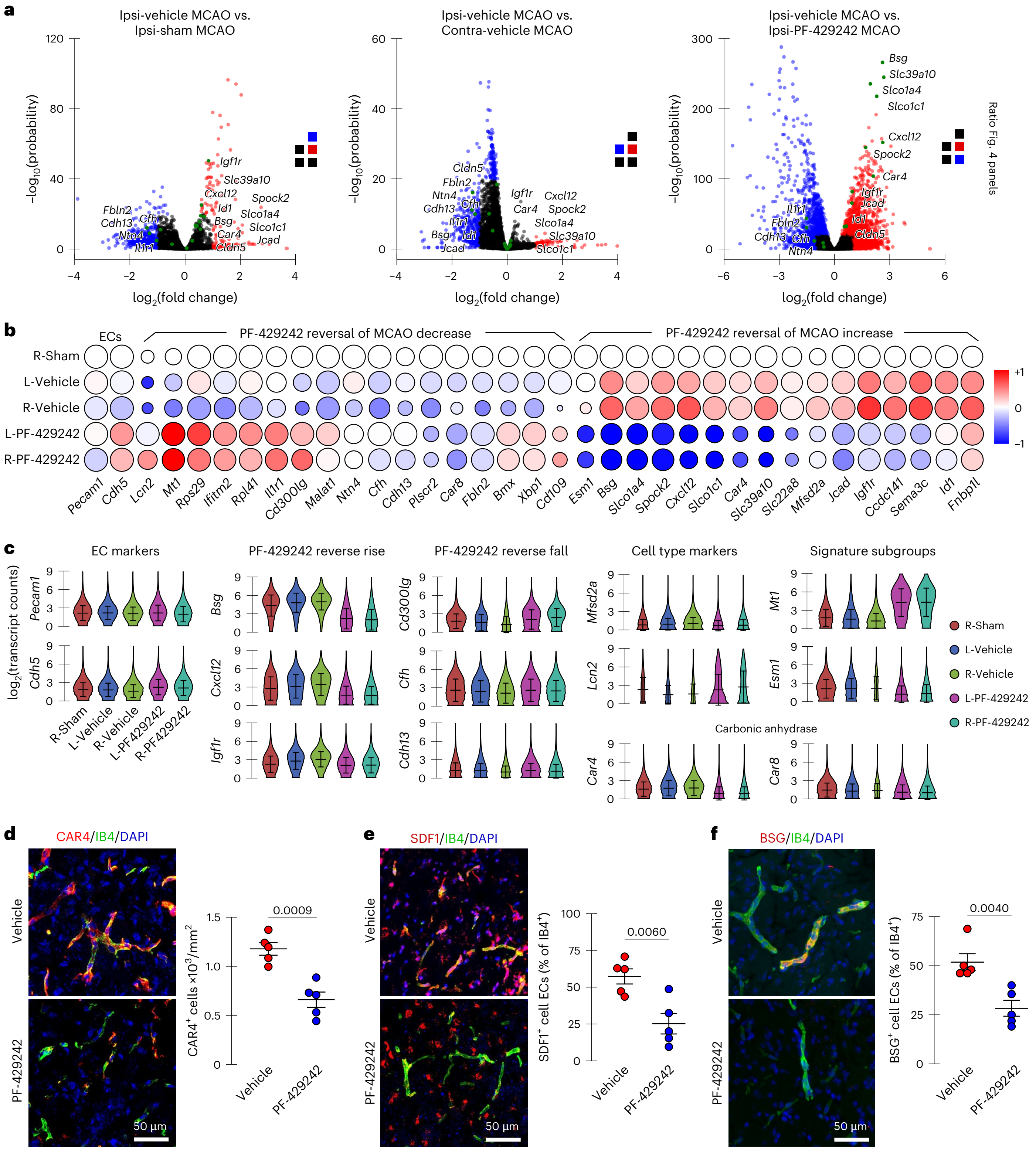

Fig. 2 | Gene expression signatures associated with PF-429242 rescue. Gene expression changes in endothelial cells due to MCAO and PF-429242 rescue identified using scRNA-seq. a, Volcano plots of total gene fold changes and probabilities in the ipsilateral untreated MCAO samples versus ipsilateral sham MCAO (left), contralateral untreated MCAO (middle) and ipsilateral PF-429242-treated MCAO (right). **b**, Summary of individual gene expression differences among five conditions. Size indicates proportion of cells, and color indicates $\log_2$ fold change relative to R-Sham. **c**, Violin plots of gene expression for markers of interest (sample mean ± s.d. overlaid). **d**, Stain for carbonic anhydrase (CAR4) and isolectin (IB4) in ipsilateral MCAO cortical tissue quantified with CAR4$^+$ cell density. **e**,**f**, Stain for CXCL12/SDF1 and BSG/CD147, respectively, against IB4 in ipsilateral MCAO cortical tissue. Quantification: percentage of IB4$^+$ cells that are also CXCL12$^+$ and BSG$^+$, respectively. All graphs indicate mean ± s.e.m. Each dot represents an independent experiment. Significance in **d**–**f** was assessed with two-tailed unpaired *t*-tests. EC, endothelial cell.

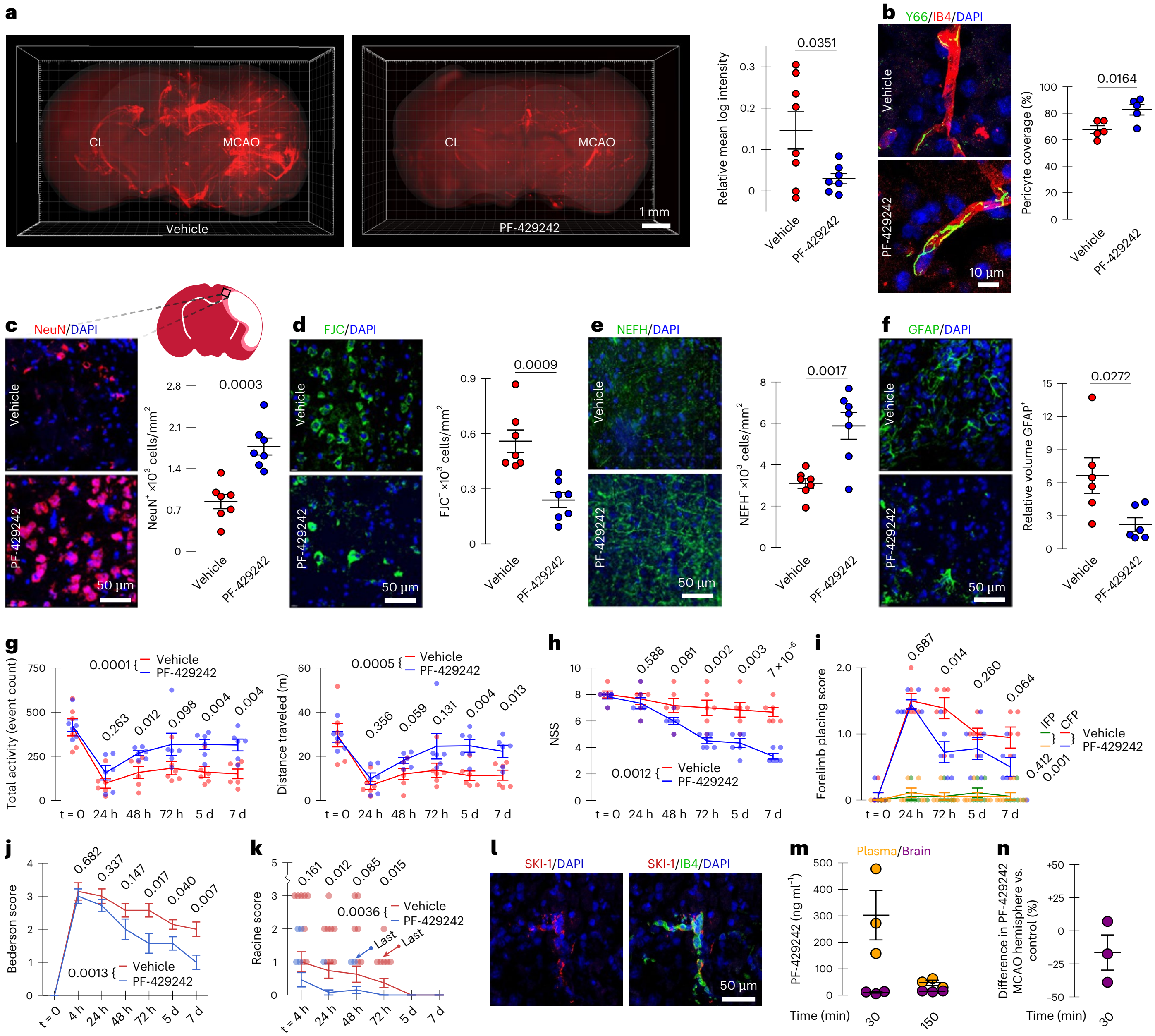

Fig. 3 | MCAO-induced BBB disruption is reduced by treatment with SKI-1 inhibitor PF-429242. **a**, LSM imaging and corresponding quantification of LSM dye leakage in the ipsilateral cortex versus contralateral control in vehicle-treated (*n* = 8) and PF-429242-treated (*n* = 7) mice 48 hours after MCAO. **b**, Pericyte coverage of endothelial cells was done by staining pericytes with a desmin antibody (Y66) and an endothelial cell marker (IB4). Quantification shows that PF-429242 treatment significantly restores coverage. Each point represents the coverage for one brain. **c**–**f**, Confocal imaging and quantification of markers in peri-infarct area of vehicle-treated and PF-429242-treated mice 7 days after MCAO. **c**, NeuN$^+$ neurons (*n* = 7 for each group). **d**, FJC$^+$ degenerating cells (*n* = 7 for each group). **e**, NEFH$^+$ cells (*n* = 7 for each group). **f**, GFAP$^+$ astrocytes (*n* = 6 for each group). **g**, Open field assessment for total activity and distance traveled. **h**,**i**, NSS and forelimb placing scores, respectively, evaluated until 7 days after MCAO. **j**,**k**, Neurological deficit and seizure activity after stroke assessed using Bederson and Racine scoring systems, respectively. Neurological scores **h**,**j** improved in PF-429242 3–7 days after MCAO, relative to their respective controls. The Racine scores **k** improved in 24 hours and 72 hours after MCAO. **l**, Confocal imaging of SKI-1 in isolectin (IB4)-positive endothelial cells. **m**, Concentration of PF-429242 in the plasma and brain 30 minutes and 150 minutes after intravenous injection of PF-429242, indicating that PF-429242 does not cross the BBB. **n**, Difference of PF-429242 found in MCAO hemisphere relative to the contralateral hemisphere shows that MCAO does not change PF-429242 levels in the brain. Therefore, the drug action is likely mediated through endothelial cells (that is, not initiated within brain). All graphs indicate mean ± s.e.m. Significance of **b**–**f** was assessed with two-tailed unpaired *t*-tests. Each dot represents an independent experiment. Time series **g**–**j** were assessed with repeated-measures factorial ANOVAs (between-group *P* values in the legends), and two-tailed unpaired *t*-tests were applied to individual timepoints. Each dot represents an independent experiment for a given timepoint. Time series **k** was assessed with a two-tailed unequal-variance *t*-test applied to cumulative subject scores (*P* value in the legend) and similarly for individual timepoint scores. Each dot represents a subject with non-zero score at a given timepoint. **m** and **n** do not assess significance.

PF-429242 benefits likely result from an effect on the BBB

According to the Human Protein Atlas, SKI-1 is expressed by human liver endothelial cells[26].

In the mouse brain, we found strong SKI-1 co-localization with isolectin-labeled endothelial cells, whereas expression in the brain parenchyma was minimal (Fig. 3l and Extended Data Fig. 1e).

Although SKI-1 is poorly expressed in neural cells, we considered whether PF-429242 might affect neurons or glia. To test this, we conducted a brain and plasma exposure study in mice. Male CD-1 mice ($n = 3$ per timepoint) received intraperitoneal PF-429242 and were euthanized at 30 minutes and 2.5 hours for liquid chromatography–tandem mass spectrometry (LC–MS/MS) analysis. At 30 minutes, plasma levels were 28.4 ± 11.0× higher than brain levels (302.4 ± 93.6 versus 10.7 ± 2.5 ng ml^{-1}; Fig. 3m). At 2.5 hours, the difference decreased to 3.2 ± 0.7× (47.3 ± 9.8 versus 15.0 ± 1.1 ng ml^{-1}). In MCAO mice, drug levels were similar in both hemispheres, with the MCAO side only 16.4 ± 13.3% lower than control (Fig. 3n). The low brain concentrations suggest that PF-429242 does not cross the BBB in sufficient amounts to directly affect neurons or glial cells.

These results support the idea that PF-429242 promotes recovery by targeting SKI-1 in endothelial cells rather than acting directly on neural tissue.

PF-429242 restores BBB and behavioral functions in rabbits

Our data show that PF-429242 repaired the BBB after MCAO in mice. Although commonly used to study ischemic injury, this mouse model does not perfectly emulate the effects of human stroke[27]. The rabbit embolic clot model, which mimics human pathology and was used to test tissue plasminogen activator (tPA), the only ischemic stroke treatment approved by the Food and Drug Administration (FDA), is a better translational model[28].

We tested PF-429242-mediated SKI-1 inhibition in this FDA-validated rabbit model[28]. Due to its complexity, many laboratories abandoned this model; we reestablished it with guidance from William C. Culp (University of Arkansas). Clot placement was confirmed by computed tomography angiography (Fig. 4a), and physiological parameters were monitored for consistency (Extended Data Fig. 7a–h). Rabbits with incorrect clot placement were excluded.

Immediately after clot placement, rabbits received daily intravenous injections of 10 mg kg^{-1} PF-429242 for 7 days (intraperitoneal injection not possible in rabbits). Magnetic resonance imaging (MRI) at 48 hours after occlusion showed a significant reduction in infarct volume in treated rabbits compared to controls ($P = 0.0014$; Fig. 4b). Due to their size, laser scanning microscopy (LSM) was not feasible, so we used dynamic contrast-enhanced (DCE) MRI with Patlak model analysis[29], confirming significantly reduced BBB leakage in PF-429242-treated rabbits ($P = 0.0073$; Fig. 4c).

Seizures occurred in three control rabbits (Racine scores 2.4 ± 0.1 at 6 hours, 2.0 ± 0.2 at 24 hours, 1.3 ± 0.2 at 48 hours and 1.3 ± 0.1 at 72 hours) but in only one treated rabbit (Racine scores 2.3 ± 0.3 at 6 hours, 2.0 ± 0.1 at 24 hours, 1.7 ± 0.3 at 48 hours and 1.3 ± 0.3 at 72 hours). Mortality was 21.4% overall: two of seven in the control group and one of seven in the treated group ($n = 5$ control, $n = 6$ treatment after deaths). All died within 40 hours after embolization, precluding MRI. Mortality difference was not significant ($P = 0.51$). TTC staining after 7 days of daily PF-429242 showed a significant infarct volume reduction ($P = 0.0053$; Fig. 4d). Behavioral tests showed significant neurological function restoration (Fig. 4e). Treatment did not affect body weight (Extended Data Fig. 7i).

Together, these data indicate that PF-429242's SKI-1 inhibition similarly benefits infarcted tissue and functional recovery in both rabbits and mice.

RGMa cleavage is necessary to induce blood vessel leakage

Recent studies revealed that silencing of the extracellular protein RGMa protects from blood vessel leakage after stroke[4]. We previously demonstrated that RGMa requires activation by the protease SKI-1 to affect on growing neurons[9]. These findings led us to hypothesize that PF-429242 promotes BBB integrity by preventing SKI-1-mediated RGMa activation.

Published data indicate increased membrane RGMa (mRGMa) levels in peripheral blood mononuclear cells after lacunar stroke[30], but it remains unclear if soluble RGMa (sRGMa) protein levels rise in stroke patient blood. To investigate, we collected blood from 83 patients with acute ischemic stroke (AIS) (37.3% female, mean age 66.0 ± 11.5 years) and 22 healthy controls (54.5% female, mean age 63.7 ± 10.8 years) (Supplementary Table 1). Groups were similar in age, sex, obesity and relevant medical history, except antiplatelet use, which was higher in patients ($P = 0.03$). Serum total sRGMa was significantly elevated in patients with AIS (median 5.4 ng ml^{-1}, interquartile range (IQR) 3.5–8.9) compared to controls (3.9 ng ml^{-1}, IQR 2.9–5.1) ($P = 0.008$; Mann–Whitney *U*-test) (Fig. 5a). Consistent with this clinical observation, serum RGMa levels increased 2 days after MCAO in mice (Fig. 5b), coinciding with BBB disruption (Figs. 3a and 4c).

RGM proteins undergo cleavage at a GDPH motif. Recent data suggest that serine proteases cleave this site[31]. Furthermore, we showed that SKI-1, a subtilisin-like serine protease, cleaves RGMa[9]. Consequently, we sought to assess the compatibility of the GDPH motif with the SKI-1 active site and determine if PF-429242 has similar affinity, permitting competitive inhibition. We docked an SKI-1 model (AlphaFold 2.0) with both PF-429242 and a 5-mer RGMa peptide (FGDPH) at a predicted catalytic pocket (Asp218, His249, Ser414). The RGMa peptide fit well, with favorable hydrogen bonds and an S-score of −8.16 kcal mol^{-1}; the cleavage site's carbonyl carbon was 3.61 Å from Ser414's oxygen, suitable for catalysis (Fig. 5c). PF-429242 occupied part of the pocket, forming an H-bond with Ser414 (2.68 Å) and had a similar S-score of −7.90 kcal mol^{-1} (Fig. 5d). Both ligand and peptide shared similar orientations (Fig. 5e), supporting competitive inhibition by PF-429242. Detailed interaction maps are shown in Extended Data Fig. 8a,b.

To confirm inhibition, we treated HEK293F cells with PF-429242 and performed western blotting for RGMa. PF-429242 treatment abolished RGMa cleavage products (Fig. 5f). Because SKI-1 cleavage sequences are poorly defined, we generated 17 RGMa alanine mutants around the cleavage site. Eleven mutants fully blocked cleavage (Fig. 5g). To determine whether RGMa cleavage is critical for its interaction with Neogenin, we performed an interaction assay in which alkaline phosphatase (AP)-tagged Neogenin interacts with RGMa-coated plates (Extended Data Fig. 9a). After washing, the binding of Neogenin–AP to RGMa proteins is revealed by the presence of the AP reporter (Extended Data Fig. 9a). Using this assay, we further demonstrated that prior RGMa cleavage is required for it to interact with Neogenin (Fig. 5h). Given Neogenin expression in endothelial cells (Extended Data Fig. 9b,c), RGMa cleavage is required for endothelial effects.

The non-cleavable RGMa point mutants, found in our alanine scan, were used to verify the specificity of native peptide docking. Two 5-mer RGMa peptides with mutations corresponding to disrupted RGMa cleavage (D149A and P150A) were docked with the SKI-1 active site as described previously for the native peptide. These mutants failed to bind the catalytic site of SKI-1 properly, confirming specificity (Extended Data Fig. 8c,d).

Finally, to test the functional impact of cleavage, we intravenously injected either sRGMa or a non-cleavable mutant (sRGMa$^{\mathrm{H151A}}$) into WT mice. After 24 hours, we assessed blood vessel leakage using TR-dextran and confocal microscopy (Fig. 5i). sRGMa significantly increased vascular leakage compared to the mutant, demonstrating that RGMa cleavage is essential for altering blood vessel integrity.

RGMa cleavage regulates proteins involved in BBB integrity

We next investigated whether SKI-1-mediated cleavage of RGMa drives the changes in endothelial cell protein expression observed with PF-429242 treatment. To test this, we compared the effects of cleaved

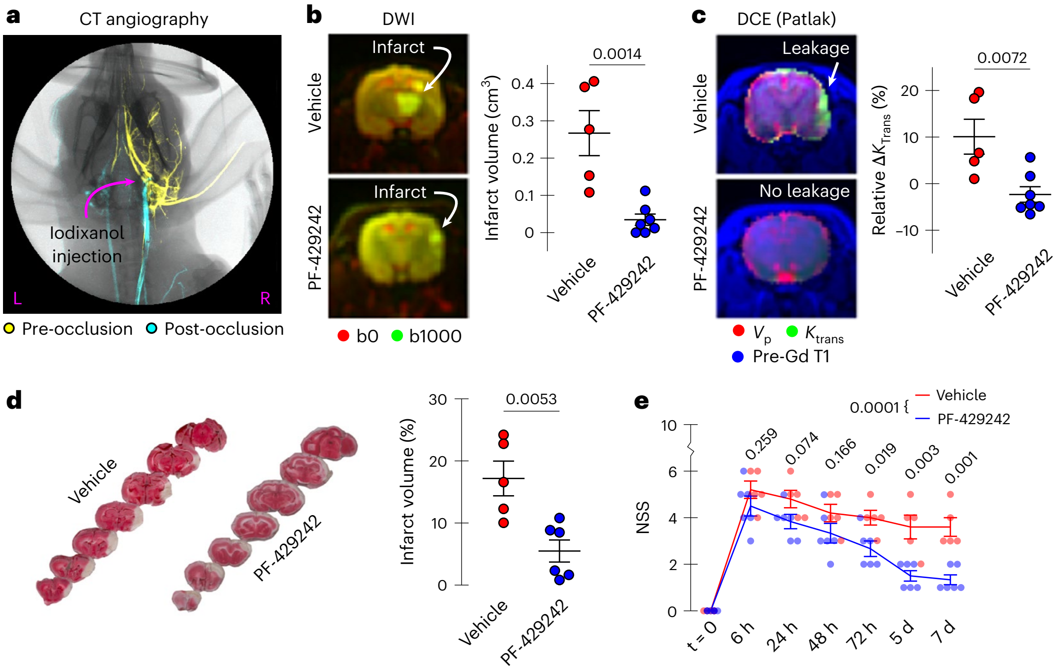

Fig. 4 | MRI of vascular disruption in rabbit stroke model confirms protective effects of SKI-1 inhibitor PF-429242. a, Angiograph of contrast agent (iodixanol) injection before and after embolization. **b**,**c**, MRI of vehicle-treated ($n = 5$) and PF-429242-treated ($n = 6$) rabbits 2 days after infarction. **b**, DWI of infarcted regions. Quantification: infarct volume computed from segmentation of b1000 hyperintense regions. **c**, Patlak modeling of vascular permeability (K_{trans}) and plasma volume (V_p) from DCE imaging of gadolinium contrast agent accumulation. Quantification: relative difference in K_{trans} values between the ipsilateral and contralateral hemispheres. **d**, TTC-stained coronal brain slices showing the representative infarcted area in vehicle-treated ($n = 5$) and PF-429242-treated ($n = 6$) rabbits. Infarcted metabolically inactive tissue appears white and was quantified using Yang's normalization scheme. **e**, NSS evaluated until 7 days after embolization. All graphs indicate mean ± s.e.m. Significance of **b**–**d** was assessed with two-tailed unpaired *t*-tests. Each dot represents an independent experiment. Time series **e** was assessed with repeated-measures factorial ANOVA (between-group *P* value in the legend), and two-tailed unpaired *t*-tests were applied to individual timepoints. Each dot represents an independent experiment for a given timepoint. CT, computed tomography; Gd, gadolinium.

RGMa and the cleavage-deficient mutant RGMa-H151A on bEnd.3 endothelial cells. We measured key BBB-related proteins, PLVAP and VE-cadherin, by western blot after treating cells with vehicle (PBS), RGMa (5 µg ml^{-1}) or RGMa-H151A (5 µg ml^{-1}). No significant differences were observed in PLVAP or VE-cadherin expression among groups (Extended Data Fig. 4c,d). Consistently, scRNA-seq showed negligible changes in VE-cadherin transcripts after PF-429242 treatment (Fig. 2c).

Next, we examined CD147/BSG, which was clearly regulated by PF-429242 (Fig. 2). Western blot analysis 24 hours after treatment revealed that RGMa, but not RGMa-H151A, significantly increased CD147 expression (Fig. 6a). This finding is notable because CD147 activates metalloproteinases (MMPs) and regulates vascular endothelial growth factor A (VEGF-A) signaling, both critical for BBB integrity[32].

We then assessed the role of RGMa cleavage in MMP2/9 activation using zymography. RGMa induced significant activation of both MMPs, whereas RGMa-H151A did not (Fig. 6b and Extended Data Fig. 4e). Additionally, when cells were treated with VEGF-A, RGMa, but not RGMa-H151A, reduced VEGF receptor 2 (VEGF-R2) protein levels compared to control (Fig. 6c). These data indicate that RGMa cleavage by SKI-1 is essential for CD147 expression and downstream activation of MMP2, MMP9 and the VEGF-A pathway.

Because angiogenic effects of RGMa on endothelial cells require the interaction of Neogenin with UNC5B, we tested the role of UNC5B in CD147 regulation. Using a neutralizing antibody against UNC5B, we found that blocking UNC5B reduced CD147 protein levels, counteracting the effect of RGMa (Fig. 6d). This reduction occurred with both RGMa and RGMa-H151A treatment, suggesting that UNC5B broadly mediates CD147 expression. We also tested Netrin, another extracellular ligand engaging UNC5B and Neogenin, for its effect on CD147. Netrin alone did not significantly affect CD147 expression compared to controls, and its effect was 51.5 ± 22.6% lower than RGMa (Extended Data Fig. 4f). Co-treatment with RGMa or RGMa-H151A plus Netrin did not significantly increase CD147 expression beyond Netrin alone, indicating that RGMa and Netrin likely share the same pathway for regulating CD147. A proposed mechanism illustrating how RGMa regulates CD147, VEGF-R2 and MMP2/9 via SKI-1 cleavage is summarized in Fig. 6e.

RGMa cleavage is necessary for blood vessel dysfunction

To investigate the importance of RGMa cleavage in blood vessel alteration after stroke, we generated a mouse mutant (RGMa^{F155A}) with a phenylalanine-to-alanine substitution at amino acid 155, producing a cleavage-resistant form of RGMa (Fig. 5). Heterozygous RGMa$^{F155A/+}$ mice appeared phenotypically normal, but western blot analysis revealed a marked reduction in RGMa cleavage compared to WT controls (Extended Data Fig. 10). Notably, no viable homozygous RGMa^{F155A} mice were born, indicating embryonic lethality similar to the observation in RGMa knockout mice, in which a defect of cephalic closure caused embryonic lethality[33].

To investigate the role of RGMa cleavage in an ischemic infarct, we performed MCAO for 1 hour in the right hemisphere of RGMa$^{F155A/+}$ and WT mice. LDF confirmed similar reperfusion between genotypes (Extended Data Fig. 2d). Vital signs and body weight loss were similar between genotypes (Extended Data Figs. 5 and 6c). Two days after MCAO, TR-dextran was intravenously injected, and animals were perfused to remove residual TR-dextran in the vessels. To assess the extent of blood leakage in the brain, we performed lightsheet imaging on iDISCO-cleared brains. As expected, the right hemisphere of MCAO WT animals displayed strong TR-dextran accumulation compared to

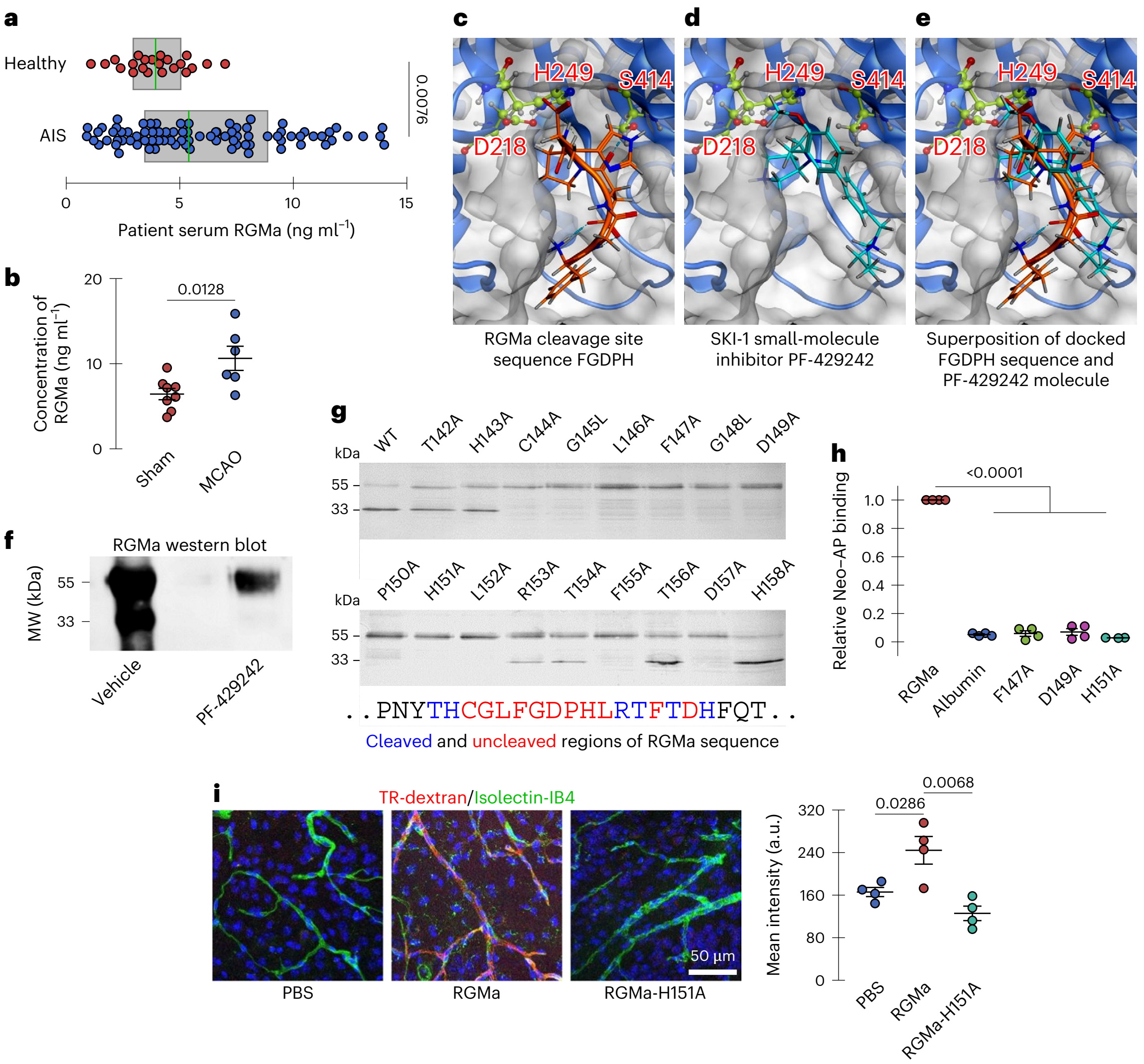

Fig. 5 | RGMa is upregulated after stroke, and RGMa cleavage inhibition prevents activation of pathways that alter BBB integrity. **a**, Human serum RGMa levels in healthy controls and patients with AIS. **b**, Mouse serum RGMa levels in MCAO and control mice 2 days after ischemic insult. **c**–**e**, Computational ligand docking with the SKI-1 active site (catalytic triad; Asp218, His249, Ser414). **c**, SKI-1 active site docking with the 5-mer peptide sequence FGDPH on RGMa cleaved by SKI-1. **d**, SKI-1 active site docking the small-molecule inhibitor PF-429242 of SKI-1 proteolytic activity. **e**, Superimposed SKI-1 active site docking results. **f**, Western blot of full-length RGMa (upper, approximately 55-kDa band) and its cleavage products (lower, approximately 33-kDa band) from HEK293F cells cultured for 4 days in either vehicle (PBS) or PF-429242 (10 μM in PBS). **g**, Western blot of RGMa mutations expressed in HEK293 cells, where the upper band is uncleaved RGMa and the lower band is cleaved RGMa, indicating which amino acids are required for cleavage (blue) and which are not (red). **h**, Relative binding of Neogenin–AP and RGMa point mutants show that RGMa cleavage is required for interaction with Neogenin. Albumin was used as a negative control. **i**, Confocal microscopy imaging of extravascular TR-dextran accumulation in brains of healthy WT mice after intravenous injection of PBS, WT RGMa or the non-cleavable point mutant RGMa-H151A. Those treated with WT RGMa, analyzed as mean fluorescence intensity, showed greater TR-dextran accumulation. In **a**, the boxes indicate the IQR, and sample median is overlaid in green. Significance was assessed with a two-tailed Mann–Whitney *U*-test. Each dot represents an individual participant. All graphs (except **a**) indicate mean ± s.e.m. Each dot represents an independent experiment. Significance in **b** and **i** was assessed with two-tailed unpaired t-tests. In **h**, a two-tailed one-sample *t*-test against a mean of 1 was used. MW, molecular weight; Neo, Neogenin.

the left side (Fig. 7a). To quantify blood vessel leakage, we measured TR-dextran intensity in the right MCAO hemisphere normalized to the left control hemisphere. The RGMa$^{F155A/+}$ animals showed a significant reduction in relative TR-dextran extravasation when compared to their WT littermates ($P = 0.015$; Fig. 7a). These results indicate that proteolytic cleavage of RGMa is essential for MCAO-induced blood vessel leakage and that blocking RGMa cleavage preserves vascular integrity after cerebral infarction.

Neogenin triggers MCAO-induced blood vessel dysfunction

RGMa exerts its effects by interacting with the transmembrane protein Neogenin. However, it remains unclear whether the impact of RGM on blood vessels is directly mediated through Neogenin or if RGMa cleavage plays a role in this activity after stroke. Neogenin is expressed by brain endothelial cells and is known to mediate RGMa-induced alterations in blood vessel function in WT mice[11]. We now show that CD31-labeled endothelial cells continue to express Neogenin after MCAO (Extended Data Fig. 9b). Combined with data demonstrating that RGMa interacts with Neogenin to impair blood vessel integrity, these findings suggest that RGMa disrupts vessel integrity through its interaction with Neogenin. Because RGMa cleavage is required for its interaction with endothelial-cell-expressed Neogenin and consequent blood vessel disruption (Fig. 5h), we hypothesized that knocking out Neogenin in endothelial cells would restore vessel integrity after stroke.

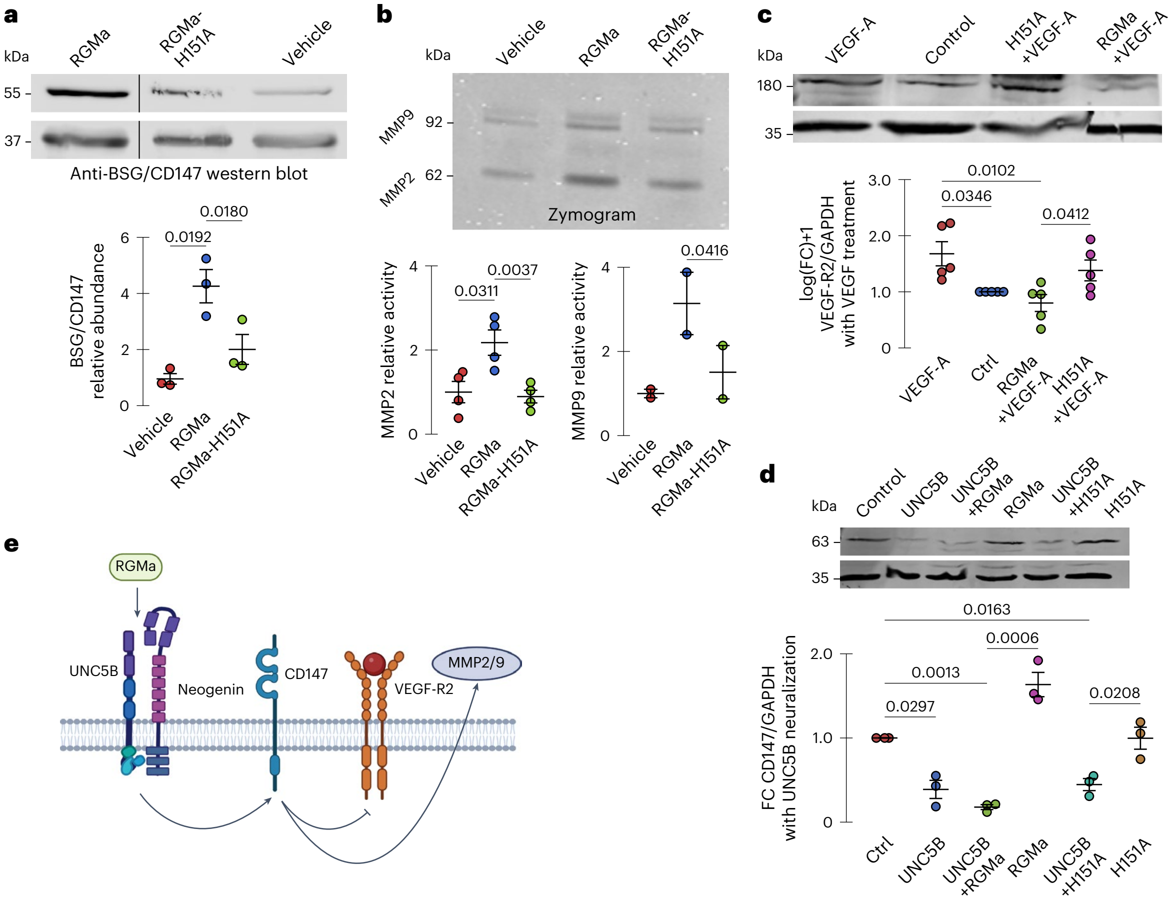

Fig. 6 | Mechanism of action of RGMa. **a**, Western blot analysis of endothelial cells (bEnd.3) treated for 24 hours with RGMa (0.5 µg ml^{-1}) shows an increase in BSG/CD147 expression when compared to vehicle-treated cells. RGMa-H151A does not induce any significant increase of BSG/CD147 expression. **b**, Zymograph of endothelial cells treated overnight with RGMa shows an increase in MMP2/9 expression when compared to vehicle-treated cells. RGMa-H151A does not induce any significant increase of MMP2/9 expression. **c**, Western blotting analysis of endothelial cells (bEnd.3) treated for 24 hours with VEGF and RGMa (0.5 µg ml^{-1}) shows that RGMa suppresses the VEGF-induced upregulation of VEGF-R2 by VEGF. RGMa-H151A does not block upregulation of VEGF-R2 by VEGF. **d**, Western blotting analysis of endothelial cells (bEnd.3) treated for 24 hours with anti-UNC5B (0.5 µg ml^{-1}) shows a decrease in BSG/CD147 expression when compared to vehicle-treated cells. RGMa-induced increase of BSG/CD147 levels is suppressed by the presence of UNC5B. RGMa-H151A does not induce any significant increase in BSG/CD147 expression. **e**, Schematic representation of the regulation of VEGF and MMP2/9 by RGMa. RGMa interacts with UNC5B and Neogenin to upregulate CD147, which increases MMP2/9 levels and decreases VEGF-R2 levels (https://BioRender.com/kp25vlc). All graphs indicate mean ± s.e.m. Each dot represents an independent experiment. Significance was assessed using two-tailed unpaired (or paired against normalization controls) *t*-tests. FC, fold change.

To test this, we used *Neo*$^{\Delta\text{Tie2-creERT2}}$ (*Neo*$^{\text{fl/fl}}$;Tie2-creERT2) conditional knockout animals, where Neogenin was genetically deleted from endothelial cells upon tamoxifen induction (TAM^{+}). LDF recordings show that *Neo*$^{\Delta\text{Tie2-creERT2}}$ animals receiving either vehicle (control/TAM^{-}) or TAM treatment 2 weeks before MCAO showed similar reperfusion after MCAO (Extended Data Fig. 2e). Vital signs and body weight loss were similar between groups (Extended Data Figs. 5 and 6d). Examination of blood vessel leakage revealed that endothelial-specific Neogenin deletion significantly reduced TR-dextran accumulation in the infarcted hemisphere ($P = 0.008$; Fig. 7b). Thus, similar to the effects seen with non-cleavable RGMa mutants, conditional deletion of Neogenin in endothelial cells markedly decreased blood vessel disruption after MCAO. Taken together with prior evidence of cleaved RGMa–Neogenin interaction, these results suggest that the binding of cleaved RGMa to Neogenin contributes to blood vessel integrity loss and that PF-429242 improves vessel function by preventing RGMa cleavage and subsequent Neogenin association.

RGMa–Neogenin interaction triggers cellular damages

Blood vessel preservation after MCAO should prevent the extravasation of toxic blood components, thereby protecting the brain. To assess the role of RGMa cleavage on the volume of cerebral infarction, we performed TTC staining[10]. Seven days after MCAO, infarct volume was reduced by 75.6 ± 5.3% ($P = 0.0002$) in RGMa$^{\text{F155A/+}}$ mice compared to WT control animals: infarct volume in control and RGMa$^{\text{F155A/+}}$ groups was 27.0 ± 3.7% and 6.6 ± 1.1% of total brain volume, respectively (Extended Data Fig. 3g,h). Similarly, edema size was significantly reduced by 51.7 ± 14.2% in RGMa$^{\text{F155A/+}}$ mice compared to control mice ($P = 0.026$; Extended Data Fig. 3i).

We next examined whether preventing RGMa cleavage protects the brain at the cellular level. RGMa$^{\text{F155A/+}}$ mice exhibited an 83.2 ± 31.5% ($P = 0.004$) increase in NeuN^{+} neuronal cells in the peri-infarct region compared to control littermates (Fig. 7c). This neuronal preservation was attributed to reduced cell death, as FJC, a marker of degenerating neurons[10], was reduced by 62.4 ± 10.9%

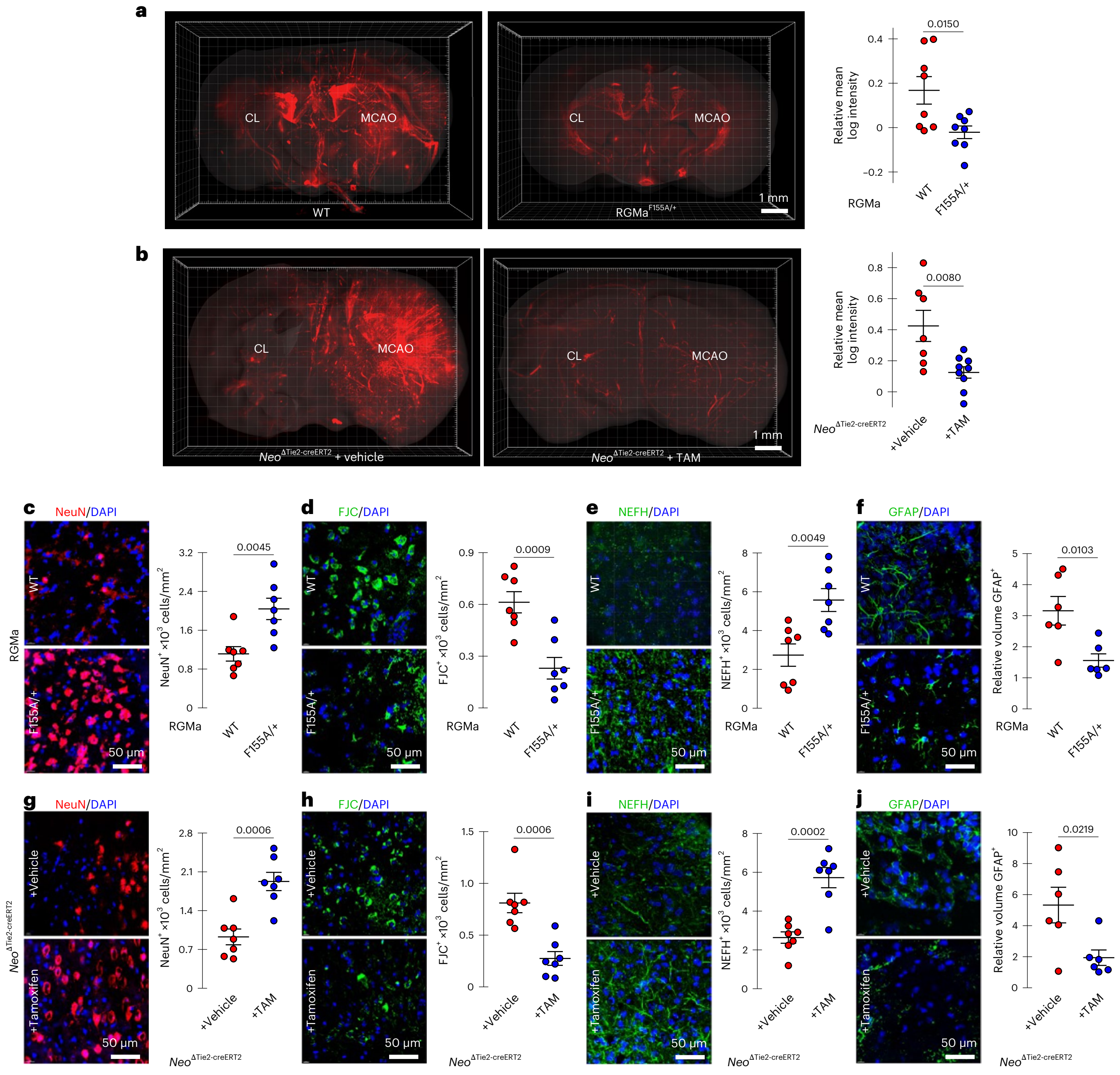

Fig. 7 | MCAO-induced blood vessel disruption and cellular damage are reduced in RGMa cleavage mutants and endothelial-specific Neo-KO mice. a, LSM imaging and corresponding quantification of MCAO-associated vascular leakage of TR-dextran in the ipsilateral cortex versus contralateral control of WT ($n = 8$) and RGMa$^{F155A/+}$ ($n = 8$) mice. **b**, LSM imaging and quantification of MCAO-associated vascular leakage in the ipsilateral cortex versus contralateral side of vehicle-induced ($n = 7$) and TAM-induced *Neo*$^{\Delta Tie2\text{-}creERT2}$ ($n = 9$) mice. **c**–**f**, Confocal imaging of markers in peri-infarct area of WT and RGMa$^{F155A/+}$ mice. **c**, NeuN$^+$ cells. Quantification: density of neurons ($n = 7$ for each group). **d**, FJC$^+$ cells ($n = 7$ for each group). Quantification: density of degenerating neurons. **e**, NEFH$^+$ cells ($n = 7$ for each group). Quantification: density of neurofilament-positive cells. **f**, GFAP$^+$ cells ($n = 6$ for each group). Quantification: cell volume relative to equivalent contralateral site. **g**–**j**, Confocal imaging of markers in peri-infarct area (diagram in Fig. 3c) of vehicle-induced and TAM-induced *Neo*$^{\Delta Tie2\text{-}creERT2}$ mice. **g**, NeuN$^+$ cells ($n = 7$ for each group). Quantification: density of neurons. **h**, FJC$^+$ cells ($n = 7$ for each group). Quantification: density of degenerate neurons. **i**, NEFH$^+$ cells ($n = 7$ for each group). Quantification: density of neurofilament-positive cells. **j**, GFAP$^+$ cells ($n = 6$ for each group). Quantification: cell volume relative to equivalent contralateral site. All graphs indicate mean ± s.e.m. Each dot represents an independent experiment. Significance was assessed using two-tailed unpaired *t*-tests. KO, knockout; CL, contralateral; Neo, Neogenin.

($P = 0.0009$; Fig. 7d). Given the preservation of neurons in RGMa$^{F155A/+}$ mice after MCAO, we then investigated whether the axonal network was similarly preserved. To this aim, NEFH immunostaining[10] was examined in the peri-infarct region (Fig. 7e). The number of NEFH$^+$ cells was significantly increased by 103.7 ± 48.0% ($P = 0.005$) in RGMa$^{F155A/+}$ mice compared to WT, indicating preserved axonal networks after injury. Consistent with observations in PF-429242-treated mice, we observed a 51.7 ± 9.9% ($P = 0.010$) decrease in GFAP$^+$ cell volume in RGMa$^{F155A/+}$ mice compared to WT (Fig. 7f). Together, these results demonstrate that inhibiting RGMa cleavage reduces infarct

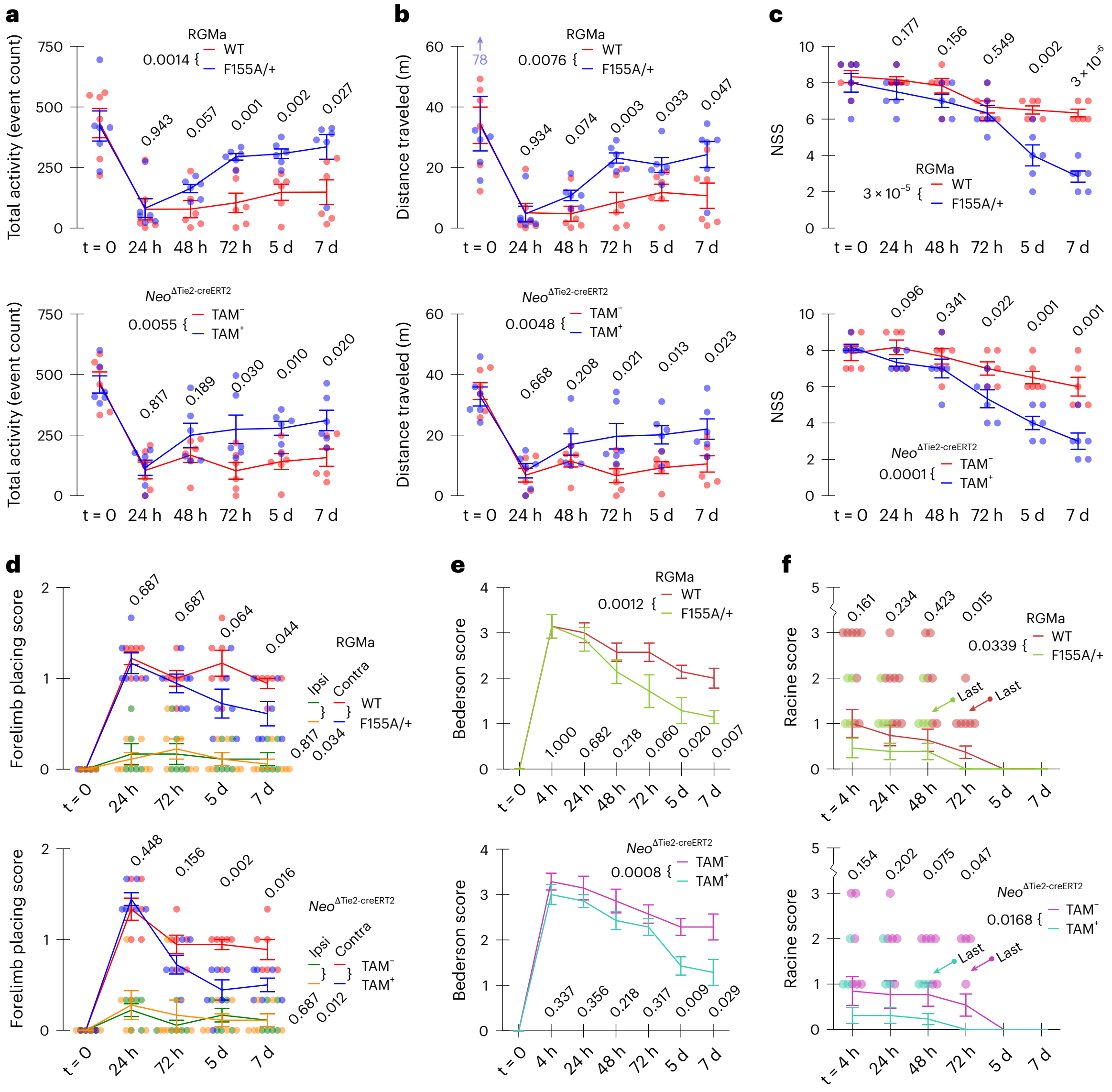

Fig. 8 | Disruption of RGMa–Neo1 signaling pathway reduced behavioral deficits observed over 7 days after MCAO. a,**b**, Open field assessment for total activity and distance traveled, respectively. Amonlite system diagram is shown in Extended Data Fig. 6b. **c**, NSS. **d**, Forelimb placing score both contralateral forelimb (controlled by infarcted ipsilateral cortex) and ipsilateral forelimb (controlled by contralateral cortex). **e**,**f**, Neurological deficits and seizure activity after stroke assessed with Bederson and Racine scoring systems, respectively. Neurological scores **c**,**e** improved in RGMa$^{F155A/+}$ and *Neo*$^{\Delta Tie2\text{-}creERT2}$+TAM groups 3–7 days after MCAO, relative to their respective controls. Racine scores **f** improved at 72 hours after MCAO. For all graphs, time indicates hours or days after MCAO, where t = 0 is prior to MCAO. All graphs indicate mean ± s.e.m. Time series **a**–**e** were assessed with repeated-measures factorial ANOVAs (between-group *P* values in the legends), and two-tailed unpaired *t*-tests were applied to individual timepoints. Each dot represents an independent experiment at a given timepoint. Time series **f** was assessed with a two-tailed unequal-variance *t*-test applied to cumulative subject scores (*P* values in the legends) and similarly for individual timepoint scores. Each dot represents a subject with non-zero score on a given day.

size, edema and astrocyte reactivity while preserving neurons and their axons after MCAO.

Next, we assessed the role of endothelial Neogenin in the same processes. Seven days after MCAO, brain infarct volume was reduced by 65.1 ± 6.7% (*P* = 0.0007) in TAM-induced *Neo*$^{\Delta Tie2\text{-}creERT2}$ mice compared to vehicle-injected control animals: brain infarct volume in control and *Neo*$^{\Delta Tie2\text{-}creERT2}$ groups was 25.8 ± 3.5% and 9.0 ± 1.2% of total brain volume, respectively (Extended Data Fig. 3g,h). Similarly, edema was significantly reduced by 63.7 ± 13.5% in *Neo*$^{\Delta Tie2\text{-}creERT2}$ mice compared to the control group (*P* = 0.003; Extended Data Fig. 3i).

Loss of endothelial Neogenin also improved neuron health in a similar manner as was observed with RGMa$^{F155A/+}$ mice. *Neo*$^{\Delta Tie2\text{-}creERT2}$ mice showed a 107.8 ± 36.6% (*P* = 0.0006) increase in the number of NeuN$^+$ neurons (Fig. 7g), a 66.1 ± 9.1% (*P* = 0.0006) reduction in FJC-labeled degenerating neurons (Fig. 7h) and a 117.2 ± 31.3% (*P* = 0.0002) increase NEFH$^+$ cells (Fig. 7i). In addition, as observed in RGMa$^{F155A/+}$ mice after MCAO, astroglial cell activation also decreased by 63.6 ± 12.2% (*P* = 0.022; Fig. 7j). Across all measured parameters (NeuN, FJC, NEFH and GFAP), similar effects were observed in PF-429242, RGMa$^{F155A/+}$ and *Neo*$^{\Delta Tie2\text{-}creERT2}$ mice. The coefficient of variation for relative changes was 0.124 ± 0.018, indicating high reproducibility. This consistency reinforces our hypothesis that preventing RGMa cleavage with PF-429242—and thereby blocking cleaved RGMa interaction with Neogenin—is critical for tissue preservation after ischemic stroke. Together, our data suggest that targeting the RGMa–Neogenin axis to restore blood vessel integrity may be a promising therapeutic strategy to protect brain tissue after cerebral infarction.

RGMa–Neogenin interaction triggers functional deficits

A battery of neurobehavioral tests for assessing sensorimotor function was performed on WT, RGMa$^{F155A/+}$, *Neo*$^{\Delta Tie2\text{-}creERT2}$+TAM and *Neo*$^{\Delta Tie2\text{-}creERT2}$+vehicle control mice subjected to MCAO. MCAO resulted in similar body weight loss in all four groups (Extended Data Fig. 6c,d). Congruent with neuron preservation observed in Fig. 7, locomotor deficits were significantly alleviated after MCAO in both experimental RGMa$^{F155A/+}$ and *Neo*$^{\Delta Tie2\text{-}creERT2}$+TAM mice compared to their respective controls (Fig. 8a,b). Distance traveled and total activity in the open field test increased by 126.7 ± 19.8% and 131.2 ± 17.6% in RGMa$^{F155A/+}$ animals and by 118.3 ± 30.7% and 102.8 ± 24.2% in *Neo*$^{\Delta Tie2\text{-}creERT2}$+TAM animals compared to their respective controls 3–7 days after MCAO (Fig. 8a,b), and the NSS improved 3–7 days after MCAO (Fig. 8c). Similarly, asymmetric impairment was significantly reduced after stroke in RGMa$^{F155A/+}$ and *Neo*$^{\Delta Tie2\text{-}creERT2}$+TAM mice. Using the forelimb placing score, we observed a significant improvement in contralateral limb function, which suggests better functioning of the infarcted hemisphere (Fig. 8d). No notable differences in function were observed in the ipsilateral forelimb, suggesting that contralateral hemispheric functioning was similar on this task between groups. As predicted, RGMa$^{F155A/+}$ and *Neo*$^{\Delta Tie2\text{-}creERT2}$+TAM mice displayed significant restoration of neurological function compared to their respective controls (Fig. 8e).

Finally, a significant reduction of seizure activity was observed the first 3 days after MCAO in RGMa$^{F155A/+}$ and *Neo*$^{\Delta Tie2\text{-}creERT2}$+TAM mice compared to their respective controls (Fig. 8f). Notably, both RGMa$^{F155A/+}$ and *Neo*$^{\Delta Tie2\text{-}creERT2}$+TAM groups stopped seizure activity earlier at 48 hours after MCAO, whereas their corresponding control groups were still experiencing seizure activity at 72 hours. Together, our data show that preventing RGMa cleavage or removing Neogenin from endothelial cells both markedly reduced neurological deficits in MCAO mice.

Mortality rate for mice and rats

In the LSM vascular leakage experiments (2 days after stroke), the mortality rate was 9.6% (5/52). Four mice died between 4 hours and 24 hours: two from the *Neo*$^{\Delta Tie2\text{-}creERT2}$ TAM^{-} group, one from the WT control-PF-429242 group and one from the RGMa$^{F155A/+}$ group. One additional mouse from the WT control-RGMa$^{F155A/+}$ group died between 24 hours and 48 hours. No deaths occurred beyond 48 hours.

In the 7-day immunostaining experiments, mortality was 8.7% (4/46). Three mice died between 4 hours and 24 hours, one from each of the following groups: WT PF-429242, WT control-PF-429242 and *Neo*$^{\Delta Tie2\text{-}creERT2}$ TAM^{-}. One mouse from the WT control-RGMa$^{F155A/+}$ group died between 24 hours and 48 hours. No deaths occurred after 48 hours.

For TTC staining at 7 days, mortality was 7.9% (3/38). One mouse from each of the *Neo*$^{\Delta Tie2\text{-}creERT2}$ TAM^{-}, TAM^{+} and WT control-PF-429242 groups died between 4 hours and 24 hours. No deaths occurred beyond 24 hours.

In the 2-day immunostaining experiments, mortality was 16.6% (2/12), with both deaths occurring between 8 hours and 24 hours in the control (vehicle) group.

For brain water content analysis at 2 days after injury, the mortality rate was 9% (1/11), with a single death in the control group between 3 hours and 8 hours.

In the liver ischemic injury study (2 days), overall mortality was 12.5% (4/32), with two deaths in the control group and two in the PF-429242-treated group, all occurring between 12 hours and 24 hours.

No mortality was observed in rats used for the retinal ischemic injury and BRB leakage experiments at 2 days.

Discussion

Currently, no clinically approved treatment exists to preserve BBB integrity after brain injuries. RGMa, an extracellular protein that opens the BBB after stroke[34], may be a therapeutic target. Our study shows that RGMa requires proteolytic cleavage by SKI-1 to interact with Neogenin and alter blood vessels. Inhibiting SKI-1 with PF-429242 after ischemia suppressed expression of proteins linked to vascular dysfunction, preserved BBB integrity and improved brain and neurological outcomes.

This provides evidence that PPCs can be targeted to prevent vascular dysfunction in the CNS. Given that most of the nine PPCs are expressed in the CNS, this therapeutic avenue remains unexplored.

BBB restoration after stroke has been demonstrated in small animal models (for example, mice and zebrafish)[3,35]. Translation to humans remains limited, emphasizing the need for validation in larger animal models.

The rabbit clot embolic stroke model is a very powerful preclinical model that paved the way for FDA approval of tPA as a stroke therapeutic[28]. Angiographic stroke models are considered very similar to human ischemic attacks as both involve blood clots that cause ischemia[27]. For this reason, this model may be considered a gold standard for the preclinical validation of any stroke treatment. In this model, PF-429242 showed effects consistent with mouse data, including preventing BBB dysfunction, reducing infarct volume and improving functional outcomes—supporting its potential as a stroke therapy.

BBB dysregulation after infarct involves dysregulation of multiple genes and pathways. Therefore, effective treatment may require targeting several pathways. RGMa activates various signaling cascades via Neogenin, including those related to cell death (for example, caspase 3 and DAPK), cytoskeletal dynamics (for example, Rho and ROCK) and BBB regulation (for example, YAP and claudin 5)[34]. RGMa also activates LMO4, which regulates hundreds of genes. Thus, the benefits of SKI-1 inhibition via PF-429242 likely stem from combined modulation of multiple pathways.

Using scRNA-seq, we found that PF-429242 alters expression of genes related to vascular function. We validated several by immunohistochemistry. PF-429242 reduced levels of CAR4, CXCL12 and basigin (CD147) in endothelial cells. CAR4, an endothelial-specific carbonic anhydrase, is upregulated after ischemic stroke[36] and promotes acidosis in endothelial cells, contributing to BBB breakdown[37]. Recent studies showed that carbonic anhydrase inhibition with pan-carbonic anhydrase inhibitors was associated with reduced tissue damage and improved behavior after stroke[38]. Inhibiting carbonic anhydrases reduces tissue damage and improves outcome in stroke and Alzheimer's models[36,38,39]. Thus, CAR4 downregulation by PF-429242 supports its role in BBB repair.

Similarly, CXCL12 reduction may protect the BBB. Blocking the CXCL12/CXCR4 axis with AMD3100 restores BBB integrity after stroke[40]. Finally, CD147 (basigin), which promotes MMP release and BBB disruption, was induced by RGMa but not by non-cleavable mutant. CD147 upregulation correlated with MMP2 and MMP9, changes absent in the mutant, reinforcing the role of SKI-1 cleavage.

Together, these findings suggest that PF-429242 prevents BBB-disrupting protein expression. Although our focus is stroke, this approach may extend to other CNS diseases, such as multiple sclerosis and Alzheimer's, where BBB dysfunction is a key pathological feature.

Methods

All animal procedures were approved by the Animal Resource & Care Committee at University Health Network (Toronto, Canada) (AUP no. 4859 and AUP no. 6394).

RGMa levels in mice

RGMa levels in mice were measured using the Quantikine Mouse/Rat RGM-A Immunoassay (R&D Systems, RGMa0). Mouse blood was collected 2 days after MCAO; the serum was collected, and 50 µl (diluted 1:1 with the manufacturer's dilation buffer) was loaded per well; and the assay was performed according to the manufacturer's instructions.

RGMa protein levels in study participants

The study was approved by the hospital's ethics board and registered in the Chinese Clinical Trial Registry (ChiCTR1800018569). Written informed consent was obtained from all participants. Eligible patients were 18 years of age or older and were diagnosed with AIS via diffusion-weighted imaging (DWI)-MRI within 24 hours of symptom onset. Exclusion criteria included hemorrhage on computed tomography, transient ischemic attacks, malignancy, organ failure, autoimmune or inflammatory conditions, infections, substance abuse or severe systemic illness. MRI and computed tomography scans were reviewed by an independent committee. Age-matched and sex-matched healthy controls with no neurological history were recruited from the hospital's physical examination center. Baseline clinical data were collected through interviews or medical records.

Blood samples were within 24 hours after stroke onset or first found abnormal as well as from healthy controls. The serum was separated within 30 minutes, and RGMa levels were measured by DuoSet ELISA kit (R&D Systems) according to the manufacturer's instructions. Absorbance at 450 nm was measured using a microplate reader (Varioskan; Thermo Fisher Scientific).

Statistical analysis was done using SPSS 23.0 software (SPSS, Inc.). Continuous variables are reported as mean ± s.d. or median (IQR). Categorical variables are expressed as numbers (percentages). Comparisons between groups were assessed using either unpaired two-tailed *t*-tests (for age and blood pressure) or a contingency table (for gender and medical history). We used Mann–Whitney *U*-tests to assess differences in blood glucose and serum RGMa levels, as these parameters are not typically normally distributed. Moreover, we sought to remove the effect of outliers in our primary measure of interest (serum RGMa levels).

Molecular docking

Molecular docking analyses were done using the Molecular Operating Environment (MOE; version 2022.02, Chemical Computing Group). MOE was selected for its established utility in docking both peptide ligands and small molecules and is widely adopted in pharmaceutical research for flexible ligand–protein docking. The structure of SKI-1 was predicted by AlphaFold Monomer version 2.0 (Q9WTZ3) and protonated for physiological pH (pH 7.4). Residues 1–186 were removed to mimic the proteolytic processing that produces catalytically competent SKI-1. The system was energy minimized using Amber10:EHT forcefield and gradient of 0.1 root mean square (RMS) kcal mol^{-1} Å^{-2}, and the SiteFinder algorithm was used to identify the binding pocket around the predicted catalytic triad (Asp218, His249, Ser414). The FGDPH peptide sequence was derived from RGMa amino acid sequence around the cleavage site and constructed with MOE protein builder. Alanine mutant peptides were prepared by the same method. The PF-429242 structure was imported from PubChem. Both ligands were protonated consistent with physiological pH, followed by energy minimization as described previously. The compounds were then docked (MOE) using the induced fit placement method, with free motion of side chains to allow for flexible docking within the pocket. The GBVI/WSA dG scoring method was used to rank the docking poses[41]. The top poses were selected based on S-scores and rational evaluation by a computational chemist. The selected poses were subjected to additional energy minimization before result quantification and rendering. Final minimized S-scores were calculated with GBVI/WSA dG. Although S-scoring is used to rank the docked poses, the docked peptides and molecules are analyzed by visual inspection to exclude outliers from the process in a logical manner, to ensure that they are indeed docking in the specified pocket, which is assumed based on conserved catalytic residues across subtilisin proteases. Poses where the cleavage site of the peptide (GDPH) was not detected in proximity to the catalytic residues (Asp218, His249, Ser414) were excluded, as these poses would not be an accurate representation of protease activity.

Generation of non-cleavable RGMa point mutant mice colony

The desired mutations for RGMa required the nucleic acid changes c.457_459AGG > GCA and c.463_464TT > GC. The additional mutation c.453 C > T was used to inactivate PAM to prevent re-cleavage of the repaired allele.

Embryos were extracted from 3–4-week-old C57BL/6NCrl (Charles River Laboratories) or C57BL/6J (The Jackson Laboratoy) female mice. CD-1/ICR mice (Charles River Laboratories) outbred albino stock were used as pseudo-pregnant recipients.

Eggs were obtained through superovulation by intraperitoneal injection of 5 IU of pregnant mare's serum gonadotropin (PMSG; Prospec, HOR-272) followed by an intraperitoneal injection of 5 IU of human chorionic gonadotrophin (hCG; EMD Millipore, 230734). Supervoluated females were then mated. Oviducts were dissected as previously described[42]. Fertilized embryos were selected prior to pronuclear microinjection or electroporation and cultured in KSOMaa and transferred into the oviducts of 0.5 days post conception (dpc) pseudo-pregnant CD-1/ICR female recipient mice shortly after manipulations[42].

To produce point mutation alleles, guide RNAs (gRNAs) were designed to target as close to the desired point mutant as possible using CRISPR[43] with specificity confirmed[44] with off-target PAM set to '-NRG'. Integrated DNA Technologies synthesized the repair template sequence (Supplementary Table 4).

Quality control was performed to ensure that there were no off-target insertions of the repair nucleotide.

Single guide RNAs (sgRNAs) were synthesized as previously described[45]; sequence AGTGGTCTGTGAAAGTCCTG was used with the CRISPR–Cas9 system. This sgRNA had a specificity score of 56 and an activity score of 0.545 and cleaved the DNA one base pair 3′ of the desired RGMa mutation site (c.458). Purified sgRNAs were analyzed on an Agilent Bioanalyzer at the Centre for Applied Genomics (Toronto, Canada) to assess integrity. Concentration was determined by Qubit with the Broad Range RNA Assay Kit (Thermo Fisher Scientific, Q10211). Electroporation mixes were prepared as previously described[46] and consisted of Cas9 protein (8 µM) and sgRNA (12 µM) in 1× buffer (100 mM KCl, 20 mM HEPES, pH 7.2–7.4).

For genotyping of H151A mutants, polymerase chain reaction was performed using RGMa primers (Supplementary Table 4). The WT sequence contains a Bsu361 restriction site, CCTCAGG, which is mutated to CCTCgca in the mutant. The WT allele was cut into fragments by Eco81I, and the mutant allele remained uncut.

Cloning and purification of soluble mouse RGMa and injection

DNA transfection and protein production protocols were inspired and modified from Aricescu et al.[47]. For sRGMa, the GPI anchor sequence was removed and SRGMa cloned into pSecTag2 B (Invitrogen, Thermo Fisher Scientific, V90020). HEK293F cells were cultured in suspension at 220 r.p.m. at 37 °C and 8% CO_2. Cells were transfected using HYPE-293 (OZ Biosciences). Cells were maintained in FreeStyle 293 Expression Medium (Gibco, 12338018; Thermo Fisher Scientific). Conditioned media were harvested 96 hours later and purified using Ni-NTA (Qiagen, 30210), and purified protein was dialyzed (Spectra/Por cellulose dialysis membrane; Spectrum Laboratories) against PBS. Protein concentrations were determined using the Bradford assay (Thermo Fisher Scientific, 23227). All point mutants were generated using site-directed mutagenesis as we did previously[9].

In injection experiments, sRGMa or RGMa-H151A was injected (50 µg in 100 µl of normal saline) via intrajugular injection 24 hours before euthanization and confocal imaging of dye (lysine-fixable TR-conjugated 70-kDa dextran) extravascular accumulation in mouse coronal brain sections.

Generation of endothelial-specific inducible Neogenin knockout mice

Neo$^{fl/fl}$ mice (provided by Jean-Francois Cloutier) were maintained on a C57BL/6J background. Endothelial-cell-specific inducible knockout mice, *Neo*$^{\Delta Tie2\text{-}creERT2}$, were generated by crossing Neo$^{fl/fl}$ with Tie2-creERT2 mice (The Jackson Laboratory, 030597). Conditional knockout mice, *Neo*$^{\Delta Tie2\text{-}creERT2}$+TAM, were given 75 mg kg^{-1} TAM between 6 weeks and 8 weeks over five consecutive days via intraperitoneal injection (20 mg ml^{-1} corn oil solution)[48]. *Neo*$^{\Delta Tie2\text{-}creERT2}$ TAM^{-} mice were given an equivalent amount of corn oil vehicle. Experiments were carried out 3–4 weeks after the last injection.

Interaction assay

The interaction assay was performed as previously described[9]. Using a 96-well microtiter plate (Corning, 3598), wells were first coated with 100 µl (10 µg ml^{-1}) of poly-L-lysine (Sigma-Aldrich, P4707 or P4832), and then 50 µl (2.5 µg ml^{-1}) of RGMa protein was added and incubated for 1 hour at 37 °C; wells were then washed three times (PBS + 0.1% Tween) and blocked with 300 µl (3% BSA in PBST). After blocking, 50 µl of AP-tagged Neogenin (produced in our laboratory) in PBS was added and incubated for 1 hour. Wells were washed three times and developed with *p*-nitrophenyl phosphate (pNPP; Sigma-Aldrich) in 100 mM $NaHCO_3$ and 1 mM $MgCl_2$. Development was stopped with 0.1 N NaOH, and absorbance was measured using a microplate reader (Agilent, BioTek EL311) at 405 nm.

Cryosection preparation and confocal imaging and immunolabeling

Animals were anesthetized and perfused with PBS followed by 4% paraformaldehyde (PFA). Brains were incubated in 4% PFA overnight, washed with PBS and left to sink in the 30% sucrose. Brains were then embedded into 30% sucrose and Optimal Cutting Temperature (OCT) compound (Tissue Plus, 4585; Fisher Health Care). Next, 20-µm cryosections (Leica, CM3050 S Cryostat) were mounted on slides and blocked with 5% BSA in PBS and then incubated with the primary antibody (antibodies listed in Supplementary Table 2). Slides were washed with PBST before incubation with secondary antibody in PBS + 10% FBS + 0.3% Triton. Slides were washed and then mounted using Dako (Agilent, CS703).

Sections were recorded using ZEN microscopy software (Zeiss, LSM 880). Pinhole was consistently set at 1.0 Airy units. Imaged regions of interest were selected from the right hemisphere, cortical layers within the stroke penumbra, adjacent to necrotic core (within approximately 250 µm from the core). The *z*-stack images were captured with 2–3% laser power and detector gain of 600–800 (a.u.)[49]. Analysis was done using ImageJ 1.53k (National Institutes of Health) with Java 17.0 and Imaris 9.9 (Oxford Instruments). Quantification and analysis of all groups was randomly assigned and blinded.

FJC labeling. Brain sections were immersed in 1% sodium hydroxide in 80% alcohol for 5 minutes, followed by 2 minutes in 70% ethanol and 2 minutes in distilled water. Slides were then transferred to a solution of 0.06% w/v potassium permanganate for 10 minutes. Slides were rinsed in water for 2 minutes and incubated for 15 minutes in FJC solution (0.0004% TR-160-FJC; Biosensis), followed by 3× 1-minute water washes and air dried. Slides were then cleared in xylene (Sigma-Aldrich, 534056) and mounted in DPX mounting medium (MilliporeSigma, 06522). The mean number of FJC^{+} neurons was calculated within the peri-infarct area.

scRNA-seq of brain endothelial cells

Isolation of FACS-sorted mouse brain endothelial cells for scRNA-seq. For FACS, cell suspensions were obtained upon digesting brain tissue in 2 mg ml^{-1} Dispase II (Sigma-Aldrich, D4693), 2 mg ml^{-1} Collagenase IV (Thermo Fisher Scientific, 1710401) and 2 mM $CaCl_2$ PBS (40 minutes at 37 °C). The suspension was filtered through 100/70/40-µm cell strainers (Corning, 431751), and cells were then centrifuged at 300*g* for 7 minutes and resuspended in 9 ml of PBS, followed by another round of centrifugation. Cell pellets were resuspended in 3 ml of ACK hemolytic buffer. To stop the reaction, 30 ml of ice-cold PBS was added and centrifuged at 300*g* for 7 minutes. Pellets were resuspended in PBS + 1% BSA. For FACS, cells were stained with anti-CD31 and anti-CD45 (Supplementary Table 3). After washes with PBS + 1% BSA, the suspension was passed through a 35-µm cell strainer of a FACS sorting tube (Corning, 352235). Cells were sorted by a FACSAria III sorter (BD Biosciences, 648282D2) using the four-way purity sorting mode. Live events were acquired and analyzed using FlowJo 10.0.6 software (Tree Star).

scRNA-seq gel bead-in-emulsion capture. FACS-sorted endothelial cells were resuspended at 1,000 cells per microliter. scRNA-seq libraries were obtained following the 10x Genomics recommended protocol using the reagents included in the Chromium Single Cell v3.3 Reagent Kit. Libraries were sequenced on a NextSeq 500 (Illumina) at the Princess Margaret Genomics Center (University Health Network, Toronto, Canada), aiming at 50,000 reads per cell. The 10x Genomics scRNA-seq data were processed using Cell Ranger version 6.1.2 with the mouse reference mm10 (GENCODE vM23/Ensembl 98).

Analysis of scRNA-seq data. Using coordinates from the Cell Ranger pipeline, transcriptomes were visualized using t-distributed stochastic neighbor embedding (t-SNE) dimensionality reduction. Similarly, *k*-means clustering with differential expression analysis was performed to identify distinct subclusters. Individual gene expression was encoded as $\log_2$ of transcript counts, and combined signatures were encoded as the geometric mean of individual encodings for concurrent visualization. Gene signatures were discovered from combinations of a reduced subset of genes, for which candidates were initially identified through highly significant *P* values associated with a one-way ANOVA applied to cellular expression levels between groups. Gene combinations, which increased the cell count ratio, were included in signatures. Potential missed candidate proteins were identified through correlation analysis of gene signature genes with genes not included in the signature.

Volcano plots were generated by computing sample fold changes ($\log_2$ of the ratio of mean transcript counts) and distribution *P* values (two-sample two-tailed *t*-test where each point is a transcript count per cell). The ipsilateral MCAO hemisphere was compared with the ipsilateral surgical sham hemisphere, the contralateral hemisphere and the PF-429252-treated ipsilateral MCAO hemisphere.

Dot plots were generated where circle area indicates the proportion of cells expressing a transcript, and deviation from white indicates the fold change (red, positive; blue, negative) relative to the ipsilateral surgical sham hemisphere.

Violin plots of gene expression were generated by smoothing a transcript count histogram ($\log_2$ scale with 6 sample binning per 2×) using a digital zero-phase low-pass RC filter.

Induction of MCAO in mice

MCAO (C57BL/6J adult male, 8–12 weeks) was carried out as previously described[50]. Anesthesia was done with 4% isoflurane with maintenance with 1.5–2% isoflurane in 30% O_2(g). After anesthesia, the skin was pulled laterally to affix a flexible microtip (Perimed, MT B500-0L240) firmly to the skull (1 mm posterior and 5 mm lateral to bregma, perpendicular to the midline) securing an LDF probe (Perimed, 418 Master probe) aligned to the middle cerebral artery (MCA), and LDF recording was done (PeriFlux System 5000 version 1.79 running PeriSoft for Windows 2.5.5; Perimed). A ventral neck incision exposed the right common carotid artery (CCA), the external carotid artery (ECA) and the internal carotid artery (ICA). The ECA was ligated distally, and a 6–0 silicone-coated monofilament (Doccol, 6023910PK10) was inserted via the ECA and advanced approximately 9–10 mm into the ICA to occlude the MCA. Regional cerebral blood flow (rCBF) was done with a transcranial laser Doppler[51]. The two collar sutures were tightened around the inserted filament. After 60 minutes, the occluding suture was withdrawn, and the right ECA was ligated at its origin. The surgical field was closed, and buprenorphine (0.05 mg kg^{-1}) was injected.

To determine circulatory parameters, we used a veterinary monitor (Bionet America, BM5VET) to measure peripheral oxygen saturation (SpO_2), systolic blood pressure (SBP), diastolic blood pressure (DBP) and mean arterial pressure (MAP) throughout the transient MCAO procedure via femoral artery cannulation (BD Intramedic, PE10). The monitor data were recorded with a VGA capture card. Additionally, we measured blood sodium and potassium concentration, blood glucose, hematocrit and hemoglobin using an i-STAT handheld analyzer (Abbott Point of Care, i-STAT1) with an i-STAT Cartridge (Abbott Point of Care, i-STAT EC4+). Blood draws were obtained via the tail vain.

Behavioral assessment

Behavioral assessment of all groups was randomly assigned and blinded.

Open field test. Mice were placed in the open field chamber for 10 minutes in a dimly lit room. An automated movement detection system (AM1053 activity monitors; Linton Instrumentation) was used to measure motor behavior in the chamber[52] (Supplementary Fig. 6). Mouse movements were tracked through beam breaks. The activity monitor software (Amonlite 1.1.31 for AM1053) was used to compute total activity and distance traveled.

Forelimb flexion test. Animals with unilateral brain damage have been found to have difficulty eliciting a placing response on the contralateral side[53]. Animals were held by their torso with the forelimbs hanging freely. The head of the mouse was kept angled upward at 45°. Contralateral and ipsilateral forelimb placing responses were induced by gently brushing the respective vibrissae on the edge of a tabletop once per trial for three trials (each side). The extending or flexing of forelimbs was scored as follows: normal behavior, immediate forelimb placement (score 0); slow or delayed placement (score 1); and placement failure within the first 2 seconds (score 2).

NSS. NSS was assessed based on the presence of reflexes and the ability to perform motor and behavioral tasks[54,55]. A point was awarded for failing to perform each of the following 10 tasks: presence of monoparesis or hemiparesis, inability to walk on a 3-cm-wide beam (repeated with 2-cm-wide and 1-cm-wide beams), inability to balance on a 1-cm-wide beam, inability to balance on a 0.5-cm-wide round stick, failure to exit a 30-cm-diameter circle after 2 minutes, inability to walk straight, loss of startle behavior and loss of seeking behavior.

Neurological deficits and seizure activity after cerebral ischemia injury. Neurological deficits and seizure activity of the mice were recorded at 4 hours, 24 hours, 48 hours, 72 hours, 5 days and 7 days after ischemic injury by a blinded observer. Neurological deficits and seizure activities were classified with Bederson and Racine scoring systems[10].

Quantification of brain infarct volume and edema

Isoflurane anesthetized mice were euthanized by decapitation, and brains were removed. For morphometric examination, the entire cerebrum was coronally sectioned into 2-mm slices using a mouse brain matrix (Zivic Instruments, BSMYS001-1) on ice. Coronal sections were stained using a 2% TTC solution in PBS at 37 °C for 20 minutes[56]. The 7-day timepoint was demonstrated as appropriate for the determination of infract volume from TTC staining by several studies[57]. Stained sections were scanned with a ScanJet (Hewlett Packard) flatbed scanner. Determinations of infarct volume and edema in all groups were blinded. Infarct volumes were calculated from scanned images of the coronal surfaces of brain slices, using the following formula[58]:

$$\text{Infarct\%} = \left(\left(V_{\text{infarct volume}} + V_{\text{uninjured hemisphere}} - V_{\text{injured hemisphere}}\right) / V_{\text{uninjured hemisphere}}\right) \times 100. \tag{1}$$

Brain edema was calculated by comparing the relative volume of the injured brain hemisphere to the uninjured hemisphere using the following formula[58]:

$$\text{Edema\%} = \left[\left(V_{\text{injured hemisphere}} - V_{\text{uninjured hemisphere}}\right) / V_{\text{uninjured }\textit{hemisphere}}\right] \times 100\%. \tag{2}$$

Brain water content measurement

Mice were randomly assigned into the vehicle group and the PF-429242 group (PF-429242 30 mg kg^{-1}), and the wet–dry weight method was used to quantify cerebral edema[59]. Forty-eight hours after MCAO, perfusion was done, and hemispheres were collected and weighed. Tissues were then dried at 110 °C for 24 hours and weighed. Both wet and dry weights were recorded, and the water content was expressed using the following equation:

$$\text{Brain water content\%} = 100 \times (\text{wet weight} - \text{dry weight})/\text{wet weight}. \tag{3}$$

Quantification of PF-429242 in mouse plasma and brain

MCAO and non-MCAO mice were randomly injected with a single intraperitoneal injection of PF-429242 (30 mg kg^{-1}). At 30 minutes (and 150 minutes for non-MCAO mice) after injection, blood was collected via cardiac puncture, and all animals were perfused with PBS, euthanized and their brains collected. A sensitive and selective ultra-performance liquid chromatography coupled with tandem mass spectrometry (UPLC–MS/MS) method was developed to determine the concentration of PF-429242 in plasma and brain tissues. Carbamazepine was used as the internal standard. PF-429242 and the internal standard were extracted from plasma and homogenized brains using protein precipitation. To this end, 20 µl of plasma and brain samples was precipitated with acetonitrile containing 100 ng ml^{-1} of the internal standard. After protein precipitation, the mixture was centrifuged, and the supernatant was transferred and mixed with two volumes of 0.1% formic acid. The final extracted samples were injected into the chromatographic system.

UPLC–MS/MS analysis was conducted on a Waters ACQUITY UPLC system coupled with a Xevo G2-XS quadrupole time-of-flight mass spectrometer (UPLC-Q-TOF-MS). Data acquisition and analysis were performed using MassLynx version 4.1 software. Chromatographic separation was achieved using an ACQUITY UPLC BEH C18 (1.7 µm, 2.1 × 50 mm) column with a gradient elution method. The mobile phase consisted of A (0.1% formic acid in water, v/v) and B (0.1% formic acid in acetonitrile, v/v), with a flow rate of 0.4 ml min^{-1}.

Mass spectrometry detection was carried out using electrospray ionization in positive ionization mode. The source temperature was set to 150 °C with a capillary voltage of 0.5 kV, cone voltage of 40 V, desolvation temperature of 600 °C, cone gas flow of 70 l h^{-1} and desolvation gas flow of 1,100 l h^{-1}. MS/MS acquisition with target enhancement mode was used for data acquisition.

Retinal ischemia–reperfusion and BRB leakage

Adult male Sprague Dawley rats (250–300 g; Charles River Laboratories) were kept according to the Canadian Council on Animal Care. Retinal ischemia–reperfusion was performed as described previously[60]. Under 2% isoflurane anesthesia, the optic nerve was exposed via an orbital incision, and the dural sheath was opened. The ophthalmic artery within the meningeal sheath was clamped for 30 minutes using a calibrated microvessel clamp and then released for reperfusion. Retinal blood flow reduction and reperfusion were confirmed via fundus examination. Animals received intraperitoneal injections immediately and 24 hours after injury: saline for controls and PF-429242 (30 mg kg^{-1}).

Evans blue leakage was studied 48 hours after injury as described previously[61]. Rats were anaesthetized with 2% isoflurane, and the jugular vein was exposed. Evans blue (Sigma-Aldrich, E-2129; 2% solution in saline, 0.2 ml per 100 g of body weight) was injected into the right jugular vein and allowed to circulate for 30 minutes. Rats were then transcardially perfused with PBS, and the retinas were collected and weighed. Retinas were then incubated in 400 µl of formamide for 48 hours to extract Evans blue. Then, 50 µl of the Evans blue-infused formamide was placed into a 96-well plate, and the optical density at 620 nm (OD_{620}) was measured. OD_{620} per gram of wet weight of each organ sample was calculated.

Vascular leakage in liver ischemia–reperfusion injury

Liver ischemia was done as described previously[62]. Mice (C57BL/6J, adult males, 8–12 weeks, 22–25 g) received analgesia administered via subcutaneous injection of 0.06 mg kg^{-1} buprenorphine (BUPAQ; Richter Pharma). Anesthesia was induced and maintained with 4% and 1.5–2% isoflurane in a 0.5:0.5 oxygen:air mixture (0.8 l min^{-1}), respectively. A microvascular clamp (00396-01, S&T; Fine Science Tools) was applied (30 minutes or 60 minutes) to the blood supply of the left lateral and median lobes inducing approximately 70% liver ischemia. Ischemia was confirmed by liver blanching.

Mice received intraperitoneal injections (PF-429242 30 mg kg^{-1} or vehicle) immediately after ischemic injury and again at 24 hours. Forty-eight hours after injury, mice received 200 µl of 2% Evans blue via the jugular vein, and Evans blue leakage was studied as described above[61].

Ex vivo lightsheet imaging

Mice were injected with lysine-fixable TR-dextran (Thermo Fisher Scientific, D1864) via tail vein at 48 hours after MCAO. Mice were subsequently anesthetized with isoflurane and perfused with PBS followed by 4% PFA. Brains were submerged in 4% PFA overnight and were lipid cleared using the iDISCO protocols[63]. Samples were stored in dibenzyl ether (DBE; Sigma-Aldrich, 33630) reagent upon complete optical transparency of the tissue and imaged using a lightsheet fluorescence microscope (LaVision BioTec, UltraMicroscope II) equipped with an optimized zoom body (Olympus, MVX-10) and an sCMOS camera (Andor Neo 5.5). Images were taken at 590 nm excitation wavelength at 30% laser power with ×0.63 zoom. Lightsheet microscopy images were acquired at 2.2 Hz using 250-ms exposure with each frame offset by 10-µm steps. Three-dimensional reconstructions and manipulations were done using Imaris 9.9 (Oxford Instruments).

Quantification of ipsilateral BBB breakdown after stroke from whole forebrain lightsheet fluorescence microscopy data. Whole forebrain tissue volumes were segmented from three-dimensional lightsheet imaging data through the application of an intensity threshold, manually correcting for any obvious tissue segmentation errors. The ipsilateral and contralateral sections of the tissue were computationally separated through linear interpolation of the midline through the image stack. A boundary region was applied to exclude any signal from the midline. Data were reported as differences between the ipsilateral and contralateral mean log intensity.

RGMa cleavage assessment in vitro and western blotting

RGMa cleavage was evaluated by western blot as previously described[9]. HEK293 cells (American Type Culture Collection (ATCC), CRL-1573) were seeded at 40,000 cells per 35-mm dish. Cells were maintained in DMEM medium (319-015-CL, DMEM, Multicell; 080-150, 10% FBS Multicell; 450-201-EL) and transfected, and media were collected 48 hours later and purified on Ni-NTA beads according to the manufacturer's protocols (Qiagen). Proteins were dialyzed in PBS before being used in all assays.

In western blotting, 20 µg of protein was loaded on 10% SDS-PAGE gels and separated by electrophoresis (Bio-Rad)[64]. Gels were transferred onto nitrocellulose membrane (Bio-Rad, 1620115). Membranes were blocked with 5% BSA in PBS and incubated in primary antibodies diluted in 1% BSA. Blots were washed with PBST (0.1% Tween) and incubated with secondary antibodies for 1 hour. Membranes were imaged using Odyssey Classic Blot Imager (LI-COR). Relative abundance of the protein was normalized to the loading control using ImageJ. All antibodies are listed in Supplementary Table 2.

bEnd.3 lysate collection. At 90% confluency, the bEnd.3 cells (ATCC, CRL-2299) culture media (DMEM, Multicell, 319-015-CL, 10% FBS Multicell) were changed to starvation media (DMEM). Treatments—with RGMa or RGMa-H151A (5 µg ml^{-1}) together with either UNC5B neutralizing antibody (5 µg ml^{-1}; Bio-Techne, AF1006) or Netrin-1 (5 µg ml^{-1}; R&D Systems, 1109-N1)—were done overnight. After overnight treatment, cells were then collected and lysed using a RIPA (Cell Signaling Technology, 9806S), phosphatase inhibitor (Thermo Fisher Scientific, 78420) and protease inhibitor cocktail (Cell Signaling Technology, 5871S). Lysate was spun in a centrifuge at 25,000 r.p.m. for 30 minutes at 4 °C. Protein concentration was calculated using a Pierce BCA Protein Assay Kit. Western blot was performed as previously described. Antibodies are presented in Supplementary Table 2.

PF-429242 of RGMa in HEK293F cells. HEK293F cells (Thermo Fisher Scientific, 11625019) were maintained in FreeStyle 293 Expression Medium (Gibco, 12338018; Thermo Fisher Scientific). Cells were shaken at 220 r.p.m. (37 °C in 8% CO_2). When cells reached 1.2×10^6 cells per milliliter, sRGMa-expressing plasmid was transfected with HYPE-293 (OZ Biosciences) and treated with PF-429242 10 µM or vehicle (PBS). Supernatant was collected 3 days after treatment, and sRGMa was purified using Ni-NTA (Qiagen, 30210).

Gel zymography

Supernatant from RGMa-treated bEnd.3 cells (ATCC, CRL-2299) was collected and concentrated using 10-kDa Amicon ultrafilters (Sigma-Aldrich, UFC801024). Then, 20 µg of protein was mixed with 6× Laemmli buffer and loaded into a 7.5% acrylamide gel + 4 mg ml^{-1} porcine gelatin. Gels were shaken in 2.5% Triton X-100 for 30 minutes twice, rinsed with 1% Triton X-100 and stained the next day with Coomassie brilliant blue. Gels were then destained in destaining solution (40% methanol, 10% acetic acid). An independent Coomassie stain was done and imaged with Odyssey Classic Blot Imager (LI-COR) to confirm equal protein loading.

Rabbit stroke model

Male New Zealand white rabbits (Charles River Laboratories), weighing 3.0–3.7 kg (16–20 weeks), were handled according to the Canadian Council on Animal Care. Two days before embolization, 1 ml of blood was taken from the rabbit's auricular vessel. The blood was mixed with 250 µl of thrombin (10 NIH U µl^{-1}; Sigma-Aldrich, T4648) and transferred into a PE 200 tubing (diameter inside, 1.4 mm; BD Intramedic) and stored at 4 °C. The form and size of the clot was checked under a microscope and washed in 0.9% saline[27,65].

Thromboembolic stroke model induction. A performed blot clot (4 mm length × 1.4 mm diameter) was injected into the MCA via the internal carotid artery[27]. Clot delivery was performed using a small animal operating station (Harvard Apparatus). Rabbits were sedated with acepromazine 1 mg kg^{-1} and buprenorphine 0.05 mg kg^{-1} via intramuscular injection and anesthetized with isoflurane (5% induction, 2% maintenance; 0.8 l min^{-1} oxygen flow rate). Physiological parameters were monitored (Bionet America, BM5VET veterinary monitor) and recorded (VGA capture card), including heart rate, respiratory rate, body temperature, peripheral oxygen saturation, intraarterial blood pressure via ear artery and electrocardiogram.

A cut was made along the right common femoral artery and its vascular sheath to introduce an angiographic catheter (3-Fr guiding catheter; Angiodynamics) and hydrophilic coated introducer sheath (4-Fr Glidesheath catheter; Terumo). The catheter was advanced from the femoral artery toward the ICA. An autologous embolus was delivered to the distal portion of the ICA[27,66]. For delivery, the catheter was flushed with 1 ml of normal saline. Angiography was conducted by injecting 1–2 ml of diluted contrast agent (iodixanol 270; GE Healthcare) to assess embolus placement and vascular occlusion. We used C-arm digital subtraction angiography (OEC 9900; GE Healthcare) to assess the movement of the contrast agent. The treatment group received 10 mg kg^{-1} PF-429242 administered via auricular vein injection every 24 hours for 7 days starting immediately after embolization.

MRI experimentation. Forty-eight hours after embolization, rabbits were sedated using acepromazine 1 mg kg^{-1} and buprenorphine 0.05 mg kg^{-1}, and anesthesia was maintained via mechanical ventilation of inhalant 1.8% isoflurane.

MRI was done using a 1.5-Tesla MRI system (Aera; Siemens Healthineers). A Siemens special-purpose radiofrequency receiver coil was positioned above the head for sensitive reception. Imaging included anatomical T2-weighted FLAIR imaging (SPACE, 0.8 × 0.8 × 1-mm resolution); DWI for infarct quantification (RESOLVE DW-EPI, 0.8 × 0.8 × 2-mm resolution; b-values 0 s/mm^2 and 1,000 s/mm^2); and pre-contrast T1 mapping (3D-VIBE, variable flip angle technique; 0.8 × 0.8 × 2-mm resolution; 2°, 9° and 19° flip angles), combined with DCE imaging for vascular leakage assessment (3D-VIBE; 0.8 × 0.8 × 2-mm resolution; 20° flip angle; 144 repetitions; 3.9-second temporal resolution; 4.63-ms repetition time (T_R); 1.87-ms time to echo (T_E)), with full brain coverage in the axial plane and consistent imaging fields of view (15.7 × 15.7 cm) for all acquisitions to facilitate image registration.

For DCE-MRI, gadolinium contrast (Bayer, Gadovist) was delivered via ear vein cannula at a rabbit-equivalent clinical dose of 0.32 mmol kg^{-1} (ref. 67). Twenty repetitions were completed before the bolus injection.

Quantification of brain infarct volume from DWI-MRI. Infarct volumes were assessed from DWI-MRI images. Regions of infarction were manually segmented by an experienced neuroradiologist using the DWI (b1000) and apparent diffusion coefficient (ADC) images. The total infract volume was computed for each rabbit brain for between-group comparison.

Quantification of vascular leakage from DCE-MRI. Magnetization signal, $M_z(t)$, measured during DCE fast acquisition was converted to ‘dynamic’ T_1 using inversion of the FLASH signal equation[68,69],

$$M_z(t) = M_z^0 \frac{\sin\alpha\,(1 - E_1(t))}{1 - E_1(t)\cos\alpha} \tag{4}$$

where $E_1(t)$ is defined as

$$E_1(\mathrm{t}) = \exp\left(\frac{-T_\mathrm{R}}{T_1(t)}\right) \tag{5}$$

and the equilibrium magnetization, M_z^0, was computed from average pre-contrast signal, $\langle M_z(t)\rangle_{t<0}$, as follows:

$$M_z^0 = \langle M_z(t)\rangle_{t<0} \frac{1 - E_1'\cos\alpha}{(1 - E_1')\sin\alpha} \tag{6}$$

where E_1' is defined as

$$E_1' = \exp\left(-\frac{T_\mathrm{R}}{T_1'}\right) \tag{7}$$

and $T_1{}'$ corresponds to the endogenous ‘static’ T_1, acquired prior to DCE using conventional imaging parameters (that is, not using the FLASH signal equation). From the time series of $M_z(t)$ after contract, $0 \le t$, we compute $E_1(t)$ using,

$$E_1(t) = \frac{M_z^0 \sin\alpha - M_z(t)}{M_z^0 \sin\alpha - M_z(t)\cos\alpha} \tag{8}$$

and then dynamic $T_1(t)$ using the inverted definition of $E_1(t)$ from equation (5),

$$T_1(\mathrm{t}) = \frac{-T_\mathrm{R}}{\ln E_1(t)} \tag{9}$$

and the concentration, $C(t)$, using the relation,

$$C(t) = \frac{1}{r_1}\left(\frac{1}{T_1(\mathrm{t})} - \frac{1}{T_1'}\right) \tag{10}$$

where r_1 is the contrast agent relaxivity, which is 5.3 s^{-1} × mM^{-1} for our contrast agent (Gadovist, 1 mmol ml^{-1}) in blood at 37 °C and 1.5 Tesla.

The voxel-wise concentration time series were fit to the Patlak compartment model[29],

$$C_\mathrm{tissue}(t) = v_\mathrm{plasma} C_\mathrm{plasma}(t) + K^\mathrm{trans}\int_0^t C_\mathrm{plasma}(\tau)\,d\tau \tag{11}$$

where $C_\mathrm{tissue}(t)$ corresponds to any voxel inside the CNS, and $C_\mathrm{plasma}(t)$ is a select voxel most closely representing the first-order decay dynamics of the contrast magnetization signal expected for blood, which was typically found in the sagittal sinus in our experiments. Converting the integral into a time series allows the Patlak model square error to be minimized using multivariant Newton optimization. The voxel-wise optimization parameters are v_{plasma} and K^{trans}, the latter directly reflecting vascular permeability.

Quantification of infract volumes and edema using TTC staining in rabbits. Seven days after embolization, rabbits were euthanized by isoflurane anesthesia in combination with intravenous injection of a lethal dose of potassium chloride (100 mg kg^{-1}, 2 mEq ml^{-1}). Brains were removed, and 4-mm-thick coronal sections were cut using a rabbit brain matrix and then stained using a 2% TTC solution. Infarct volumes were calculated from scanned images of the coronal surfaces of brain slices as in mouse brain sections[58].

Behavior monitoring in rabbits. For the NSS, neck position, righting reflex, paw dysfunction and posture were assessed[27,70]. Normal neck position was scored as 0, with twisted position consistent with wryneck scored as 1. Righting from back within 1 second was scored as 0, within 1–5 s as 1 and more than 5 seconds as 2. Paw dysfunction, for both forelimbs and hindlimbs, was assessed based on reextension timing using the same scoring scheme as righting reflex. Posture reflex test under later push scored maintaining normal posture as 0, reduced push resistance as 1 and falling to contralateral side as 2. Seizure activity was evaluated using the Racine scoring system[10].

Reporting summary

Further information on research design is available in the Nature Portfolio Reporting Summary linked to this article.

Data availability

All data generated and analyzed in this study are available on Zenodo (https://zenodo.org/records/15843737). The scRNA-seq datasets generated and analyzed in this study are available in the Gene Expression Omnibus under accession number GSE300442. Source data are provided with this paper.

Code availability

All code used to generate the figures in this publication is available on GitHub (https://github.com/DeneRinguette/Shabanzadeh2025).

References

1. Daneman, R. & Prat, A. The blood–brain barrier. *Cold Spring Harb. Perspect. Biol.* **7**, a020412 (2015).
2. Knowland, D. et al. Stepwise recruitment of transcellular and paracellular pathways underlies blood-brain barrier breakdown in stroke. *Neuron* **82**, 603–617 (2014).
3. Martin, M. et al. Engineered Wnt ligands enable blood–brain barrier repair in neurological disorders. *Science* **375**, eabm4459 (2022).
4. Li, M. et al. Adenoviral vector-induced silencing of RGMa attenuates blood-brain barrier dysfunction in a rat model of MCAO/reperfusion. *Brain Res. Bull.* **142**, 54–62 (2018).
5. Marcinkiewicz, M., Seidah, N. G. & Chrétien, M. Implications of the subtilisin/kexin-like precursor convertases in the development and function of nervous tissues. *Acta Neurobiol. Exp. (Wars.)* **56**, 287–298 (1996).
6. Seidah, N. G. & Prat, A. The biology and therapeutic targeting of the proprotein convertases. *Nat. Rev. Drug Discov.* **11**, 367–383 (2012).
7. Bell, A. S., Wagner, J., Rosoff, D. B. & Lohoff, F. W. Proprotein convertase subtilisin/kexin type 9 (PCSK9) in the central nervous system. *Neurosci. Biobehav. Rev.* **149**, 105155 (2023).
8. Jaafar, A. K., Techer, R., Chemello, K., Lambert, G. & Bourane, S. PCSK9 and the nervous system: a no-brainer? *J. Lipid Res.* **64**, 100426 (2023).
9. Tassew, N. G., Charish, J., Seidah, N. G. & Monnier, P. P. SKI-1 and Furin generate multiple RGMa fragments that regulate axonal growth. *Dev. Cell* **22**, 391–402 (2012).
10. Shabanzadeh, A. P. et al. Uncoupling Neogenin association with lipid rafts promotes neuronal survival and functional recovery after stroke. *Cell Death Dis.* **6**, e1744 (2015).
11. Wang, X. F. et al. The liver and muscle secreted HFE2-protein maintains central nervous system blood vessel integrity. *Nat. Commun.* **15**, 1037 (2024).
12. Olmstead, A. D., Knecht, W., Lazarov, I., Dixit, S. B. & Jean, F. Human subtilase SKI-1/S1P is a master regulator of the HCV lifecycle and a potential host cell target for developing indirect-acting antiviral agents. *PLoS Pathog.* **8**, e1002468 (2012).
13. Lin, J.-C., Liu, T.-P., Chen, Y.-B. & Yang, P.-M. PF-429242 exhibits anticancer activity in hepatocellular carcinoma cells via FOXO1-dependent autophagic cell death and IGFBP1-dependent anti-survival signaling. *Am. J. Cancer Res.* **13**, 4125–4144 (2023).
14. Picelli, S. et al. Full-length RNA-seq from single cells using Smart-seq2. *Nat. Protoc.* **9**, 171–181 (2014).
15. Stratman, A. N. et al. Interactions between mural cells and endothelial cells stabilize the developing zebrafish dorsal aorta. *Development* **144**, 115–127 (2017).
16. Ibrahim, A. M. et al. Fibulin-2 is required for basement membrane integrity of mammary epithelium. *Sci. Rep.* **8**, 14139 (2018).
17. Joshi, M. B. et al. T-cadherin protects endothelial cells from oxidative stress-induced apoptosis. *FASEB J.* **19**, 1737–1739 (2005).
18. Parente, R., Clark, S. J., Inforzato, A. & Day, A. J. Complement factor H in host defense and immune evasion. *Cell. Mol. Life Sci.* **74**, 1605–1624 (2017).
19. Jin, R., Xiao, A. Y., Chen, R., Granger, D. N. & Li, G. Inhibition of CD147 (cluster of differentiation 147) ameliorates acute ischemic stroke in mice by reducing thromboinflammation. *Stroke* **48**, 3356–3365 (2017).
20. McCandless, E. E. et al. Pathological expression of CXCL12 at the blood–brain barrier correlates with severity of multiple sclerosis. *Am. J. Pathol.* **172**, 799–808 (2008).
21. Lindskog, S. Structure and mechanism of carbonic anhydrase. *Pharmacol. Ther.* **74**, 1–20 (1997).
22. Bernard, M., Menet, R., Lecordier, S. & ElAli, A. Endothelial PDGF-D contributes to neurovascular protection after ischemic stroke by rescuing pericyte functions. *Cell. Mol. Life Sci.* **81**, 225 (2024).
23. Schwab, J. M., Nguyen, T. D., Meyermann, R. & Schluesener, H. J. Human focal cerebral infarctions induce differential lesional interleukin-16 (IL-16) expression confined to infiltrating granulocytes, CD8$^+$ T-lymphocytes and activated microglia/macrophages. *J. Neuroimmunol.* **114**, 232–241 (2001).
24. Cardenas, A. M. et al. Pathology of callosal damage in ALS: an ex-vivo, 7T diffusion tensor MRI study. *Neuroimage Clin.* **15**, 200–208 (2017).
25. Pan, Y. et al. Inhibition of perforin-mediated neurotoxicity attenuates neurological deficits after ischemic stroke. *Front. Cell. Neurosci.* **15**, 664312 (2021).
26. MBTPS1 protein expression summary. The Human Protein Atlas. https://www.proteinatlas.org/ENSG00000140943-MBTPS1.
27. Culp, W. C. et al. Three variations in rabbit angiographic stroke models. *J. Neurosci. Methods* **212**, 322–328 (2013).
28. Zivin, J. A., Fisher, M., DeGirolami, U., Hemenway, C. C. & Stashak, J. A. Tissue plasminogen activator reduces neurological damage after cerebral embolism. *Science* **230**, 1289–1292 (1985).
29. Patlak, C. S. & Blasberg, R. G. Graphical evaluation of blood-to-brain transfer constants from multiple-time uptake data. Generalizations. *J. Cereb. Blood Flow Metab.* **5**, 584–590 (1985).
30. Parray, A. et al. Increase in repulsive guidance molecule-a (RGMa) in lacunar and cortical stroke patients is related to the severity of the insult. *Sci. Rep.* **12**, 20788 (2022).
31. Patrick, M. E. & Egland, K. A. SUSD2 proteolytic cleavage requires the GDPH sequence and inter-fragment disulfide bonds for surface presentation of Galectin-1 on breast cancer cells. *Int. J. Mol. Sci.* **20**, 3814 (2019).
32. Li, Y. et al. Extracellular vesicles maintain blood-brain barrier integrity by the suppression of Caveolin-1/CD147/VEGFR2/MMP pathway after ischemic stroke. *Int. J. Nanomedicine* **19**, 1451–1467 (2024).
33. Niederkofler, V., Salie, R., Sigrist, M. & Arber, S. Repulsive guidance molecule (RGM) gene function is required for neural tube closure but not retinal topography in the mouse visual system. *J. Neurosci.* **24**, 808–818 (2004).
34. Zhang, L. et al. RGMa participates in the blood–brain barrier dysfunction through BMP/BMPR/YAP signaling in multiple sclerosis. *Front. Immunol.* **13**, 861486 (2022).
35. Ding, J. et al. Therapeutic blood–brain barrier modulation and stroke treatment by a bioengineered FZD4-selective WNT surrogate in mice. *Nat. Commun.* **14**, 2947 (2023).
36. Lemon, N., Canepa, E., Ilies, M. A. & Fossati, S. Carbonic anhydrases as potential targets against neurovascular unit dysfunction in Alzheimer's disease and stroke. *Front. Aging Neurosci.* **13**, 772278 (2021).
37. Bulli, I. et al. Role of carbonic anhydrase in cerebral ischemia and carbonic anhydrase inhibitors as putative protective agents. *Int. J. Mol. Sci.* **22**, 5029 (2021).
38. Wang, X. et al. Methazolamide and melatonin inhibit mitochondrial cytochrome C release and are neuroprotective in experimental models of ischemic injury. *Stroke* **40**, 1877–1885 (2009).

39. Dettori, I. et al. Protective effects of carbonic anhydrase inhibition in brain ischaemia in vitro and in vivo models. *J. Enzyme Inhib. Med. Chem.* **36**, 964–976 (2021).
40. Huang, J. et al. CXCR4 antagonist AMD3100 protects blood–brain barrier integrity and reduces inflammatory response after focal ischemia in mice. *Stroke* **44**, 190–197 (2013).
41. Labute, P. The generalized Born/volume integral implicit solvent model: estimation of the free energy of hydration using London dispersion instead of atomic surface area. *J. Comput. Chem.* **29**, 1693–1698 (2008).
42. Behringer, R. *Manipulating the Mouse Embryo: A Laboratory Manual* (Cold Spring Harbor Laboratory Press, 2014).
43. Haeussler, M. et al. Evaluation of off-target and on-target scoring algorithms and integration into the guide RNA selection tool CRISPOR. *Genome Biol.* **17**, 148 (2016).
44. Hsu, P. D. et al. DNA targeting specificity of RNA-guided Cas9 nucleases. *Nat. Biotechnol.* **31**, 827–832 (2013).
45. Gertsenstein, M. & Nutter, L. M. J.Engineering point mutant and epitope-tagged alleles in mice using Cas9 RNA-guided nuclease. *Curr. Protoc. Mouse Biol.* **8**,28–53 (2018).
46. Gertsenstein, M. & Nutter, L. M. J. Production of knockout mouse lines with Cas9. *Methods* **191**, 32–43 (2021).
47. Aricescu, A. R., Lu, W. & Jones, E. Y. A time- and cost-efficient system for high-level protein production in mammalian cells. *Acta Crystallogr. D Biol. Crystallogr.* **62**, 1243–1250 (2006).
48. Intraperitoneal injection of tamoxifen for inducible Cre-driver lines. The Jackson Laboratory. https://www.jax.org/research-and-faculty/resources/cre-repository/tamoxifen.
49. Ding, X. et al. The sonic hedgehog pathway mediates brain plasticity and subsequent functional recovery after bone marrow stromal cell treatment of stroke in mice. *J. Cereb. Blood Flow Metab.* **33**, 1015–1024 (2013).
50. Ansari, S., Azari, H., McConnell, D. J., Afzal, A. & Mocco, J. Intraluminal middle cerebral artery occlusion (MCAO) model for ischemic stroke with laser Doppler flowmetry guidance in mice. *J. Vis. Exp.* https://doi.org/10.3791/2879 (2011).
51. Hamblin, M. H., Murad, R., Yin, J., Vallim, G. & Lee, J.-P. Modulation of gene expression on a transcriptome-wide level following human neural stem cell transplantation in aged mouse stroke brains. *Exp. Neurol.* **347**, 113913 (2022).
52. Jugloff, D. G. M. et al. Targeted delivery of an *Mecp2* transgene to forebrain neurons improves the behavior of female *Mecp2*-deficient mice. *Hum. Mol. Genet.* **17**, 1386–1396 (2008).
53. Schallert, T., Fleming, S. M., Leasure, J. L., Tillerson, J. L. & Bland, S. T. CNS plasticity and assessment of forelimb sensorimotor outcome in unilateral rat models of stroke, cortical ablation, parkinsonism and spinal cord injury. *Neuropharmacology* **39**, 777–787 (2000).
54. Rogers, D. C., Campbell, C. A., Stretton, J. L. & Mackay, K. B. Correlation between motor impairment and infarct volume after permanent and transient middle cerebral artery occlusion in the rat. *Stroke* **28**, 2060–2065; discussion 2066 (1997) .
55. Beni-Adani, L. et al. A peptide derived from activity-dependent neuroprotective protein (ADNP) ameliorates injury response in closed head injury in mice. *J. Pharmacol. Exp. Ther.* **296**, 57–63 (2001).
56. Yang, G.-Y., Zhao, Y.-J., Davidson, B. L. & Betz, A. L. Overexpression of interleukin-1 receptor antagonist in the mouse brain reduces ischemic brain injury. *Brain Res.* **751**, 181–188 (1997).
57. Zhang, F. & Chen, J. Infarct measurement in focal cerebral ischemia: TTC staining. In *Animal Models of Acute Neurological Injuries II: Injury and Mechanistic Assessments, Volume 2* (eds Chen, J., Xu, X.-M., Xu, Z. C. & Zhang, J. H.) 93–98 (Humana Press, 2012).
58. Yang, Y., Shuaib, A. & Li, Q. Quantification of infarct size on focal cerebral ischemia model of rats using a simple and economical method. *J. Neurosci. Methods* **84**, 9–16 (1998).
59. Zhan, C. & Yang, J. Protective effects of isoliquiritigenin in transient middle cerebral artery occlusion-induced focal cerebral ischemia in rats. *Pharmacol. Res.* **53**, 303–309 (2006).
60. Shabanzadeh, A. P., D'Onofrio, P. M., Monnier, P. P. & Koeberle, P. D. Neurosurgical modeling of retinal ischemia–reperfusion injury. *J. Stroke Cerebrovasc. Dis.* **27**, 845–856 (2018).
61. Wick, M. J., Harral, J. W., Loomis, Z. L. & Dempsey, E. C. An optimized Evans blue protocol to assess vascular leak in the mouse. *J. Vis. Exp.* https://doi.org/10.3791/57037 (2018).
62. Nocito, A. et al. Platelets and platelet-derived serotonin promote tissue repair after normothermic hepatic ischemia in mice. *Hepatology* **45**, 369 (2007).
63. Renier, N. et al. iDISCO: a simple, rapid method to immunolabel large tissue samples for volume imaging. *Cell* **159**, 896–910 (2014).
64. Western blot protocol | Abcam. https://www.abcam.com/protocols/general-western-blot-protocol.
65. Murray, V. et al. The molecular basis of thrombolysis and its clinical application in stroke. *J. Intern. Med.* **267**, 191–208 (2010).
66. Brown, A. T. et al. Stroke location and brain function in an embolic rabbit stroke model. *J. Vasc. Interv. Radiol.* **21**, 903–909 (2010).
67. Nair, A. B. & Jacob, S. A simple practice guide for dose conversion between animals and human. *J. Basic Clin. Pharm.* **7**, 27–31 (2016).
68. Cheng, H.-L. M. & Wright, G. A. Rapid high-resolution T1 mapping by variable flip angles: accurate and precise measurements in the presence of radiofrequency field inhomogeneity. *Magn. Reson. Med.* **55**, 566–574 (2006).
69. Foltz, W. et al. Phantom validation of DCE-MRI magnitude and phase-based vascular input function measurements. *Tomography* **5**, 77–89 (2019).
70. Zhao, B.-Q. et al. A novel MCA occlusion model of photothrombotic ischemia with cyclic flow reductions: development of cerebral hemorrhage induced by heparin. *Brain Res. Brain Res. Protoc.* **9**, 85–92 (2002).

Acknowledgements

This work was funded by the Canadian Institutes for Health Research (grant no. PJT 16397) (P.P.M.) and the Heart and Stroke Foundation of Canada (G240038139) (P.P.M.). The authors would like to acknowledge the contribution of the Model Production Core staff at the Centre for Phenogenomics (http://www.phenogenomics.ca/cite-tcp.html) for the generation of genetically modified models. The authors acknowledge R. Logan and J. H. Eubanks (Division of Experimental and Translational Neuroscience, Krembil Research Institute, University Health Network, Toronto, Canada) for assistance with open field experiments. We thank W. C. Culp (University of Arkansas) and R. Jahan (University of California, Los Angeles) for their time and efforts to help us reestablish the rabbit embolic stroke model. We thank the staff at the University Health Network Animal Resource Centre for their invaluable assistance in the husbandry care and surgical support and K. Ma (University Health Network, Toronto, Canada) for direct technical support and clinical guidance. We also thank B. M. Kuba (University Health Network, Toronto, Canada) for technical advice and extensive assistance in research material selection.

Author contributions

Conceptualization: P.P.M. and A.P.S. Methodology: A.P.S. and D.R. Methodology (modeling): I.M., M.R., A.M., M.M. and C.B. Methodology (imaging and scRNA-seq): W.D.F., A.P.S., D.R., L.O., S.L., S.E.S., B.Q., P.S.A. and T.W. Methodology (protein analysis): A.P.S., M.S., Q.W.,

N.G.T., E.K.M., J.F. and X.Q. Methodology (surgeries): A.P.S., M.S. and J.F. Analysis: D.R., A.P.S., M.M., W.D.F., P.A.-L. and I.M. Writing—original draft: P.P.M., A.P.S., P.L.C. and D.R. Writing—review and editing: P.P.M., D.R. and A.P.S. Funding acquisition: P.P.M. Project management: A.P.S. Supervision: P.P.M.

Competing interests

The authors declare no competing interests.

Additional information

Extended data is available for this paper at https://doi.org/10.1038/s44161-025-00691-5.

Supplementary information The online version contains supplementary material available at https://doi.org/10.1038/s44161-025-00691-5.

Correspondence and requests for materials should be addressed to Philippe P. Monnier.

Peer review information *Nature Cardiovascular Research* thanks Arne Elofsson and the other, anonymous, reviewer(s) for their contribution to the peer review of this work.

---

[1]Krembil Research Institute, University Health Network, Toronto, Ontario, Canada. [2]Krembil Brain Institute, University Health Network, Toronto, Ontario, Canada. [3]Donald K. Johnson Research Institute, University Health Network, Toronto, Ontario, Canada. [4]Department of Physiology, Faculty of Medicine, University of Toronto, Toronto, Ontario, Canada. [5]Department of Neurology, The First Affiliated Hospital of Chongqing Medical University, Chongqing, China. [6]Slaight Family Centre for Advanced MRI, Toronto Western Hospital, University Health Network, Toronto, Ontario, Canada. [7]McEwen Stem Cell Institute, University of Health Network, Toronto, Ontario, Canada. [8]STTARR Innovation Centre, Department of Radiation Oncology, University Health Network, Toronto, Ontario, Canada. [9]Department of Pharmacology and Toxicology, University of Toronto, Toronto, Ontario, Canada. [10]Group Brain Vasculature and Perivascular Niche, Department of Oncology, University College London Cancer Institute, University College London, London, UK. [11]Victor Horsley Department of Neurosurgery, National Hospital for Neurology and Neurosurgery, University College London Hospitals NHS Trust, London, UK. [12]Division of Neuroradiology, Joint Department of Medical Imaging, Toronto Western Hospital, University Health Network, University of Toronto, Toronto, Ontario, Canada. [13]Department of Ophthalmology, Faculty of Medicine, University of Toronto, Toronto, Ontario, Canada.
✉e-mail: pmonnier@uhnres.utoronto.ca

https://doi.org/10.1038/s44161-025-00691-5

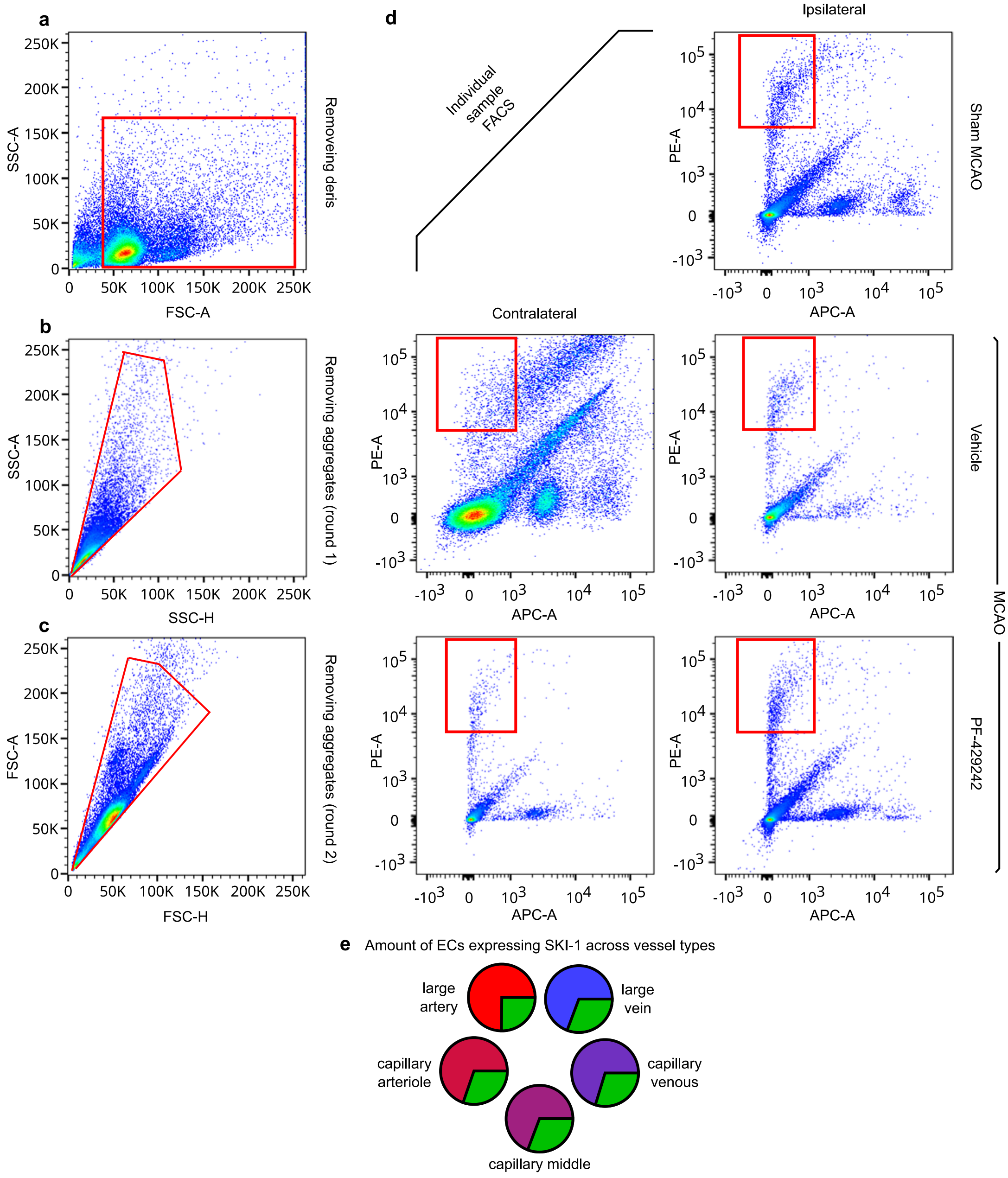

Extended Data Fig. 1 | FACS gating strategy to enrich endothelial cells and SKI-1 transcript expression. **a**, Removing debris based on SSC-A and FSC-A gaiting. **b**, Removing aggregates with SSC-A and SSC-H gaiting. **c**, Additional round of aggregate removal based on FSC-A and FSC-H gaiting. **d**, CD31+ and CD45- gaiting for ipsilateral sham MCAO hemisphere and both the ipsilateral and contralateral MCAO hemispheres in both vehicle and PF-429242 treated mice. **e**, Quantity of ECs expressing SKI-1 across vessel types. The fraction of ECs expressing SKI-1 across vessel types identified through scRNA-seq analysis are indicated by the green fraction in each pie chart. Corresponding vessel type markers indicated in Fig. 1d, g.

https://doi.org/10.1038/s44161-025-00691-5

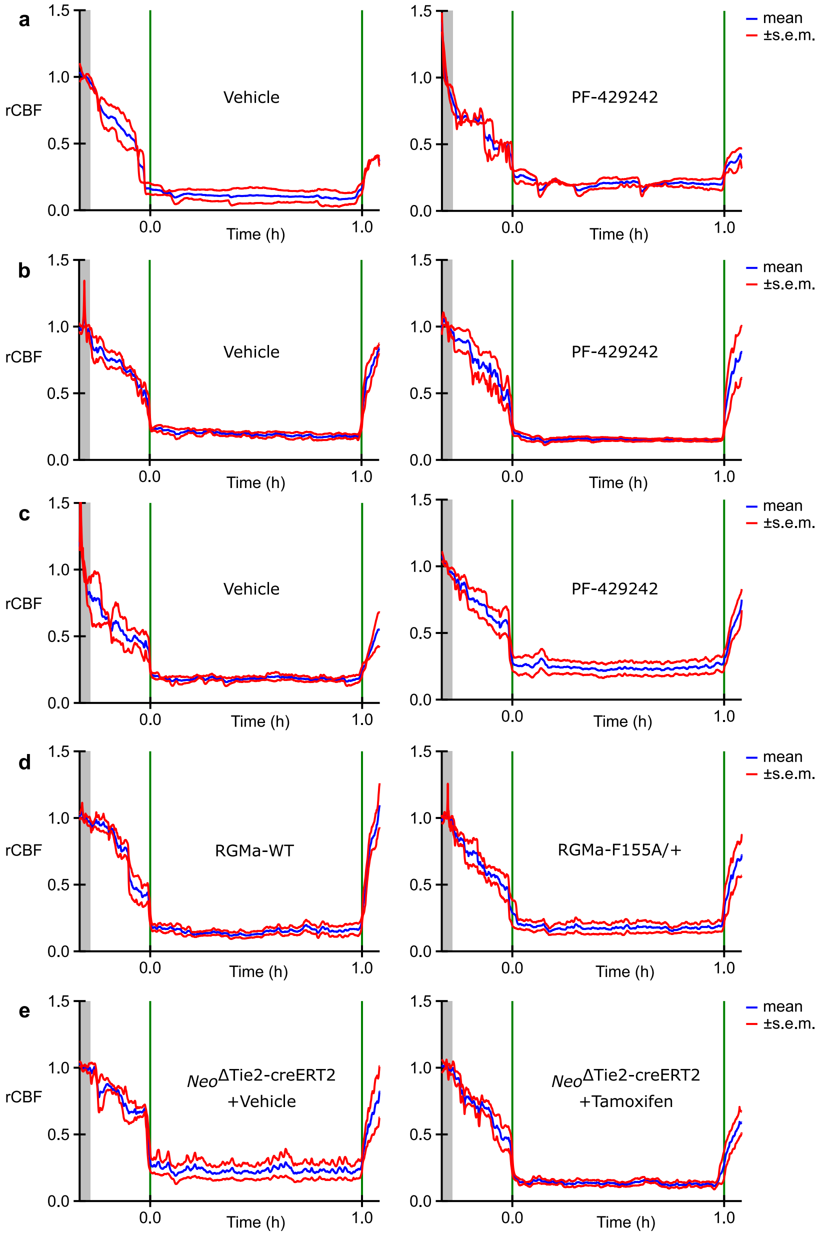

Extended Data Fig. 2 | Laser Doppler flowmetry tracking of MCAO progression in mice. a, Vehicle and PF-429242 treated mice used for scRNA-seq analysis. **b**, Vehicle and PF-429242 treated mice used for light-sheet microscopy and confocal histology. **c**, Vehicle and PF-429242 treated mice used for assessing brain water content. **d**, WT and RGMa-F155A/+ mice used for light-sheet microscopy and confocal histology. **e**, Vehicle- and tamoxifen-treated *Neo*$^{\Delta\text{Tie2-creERT2}}$ mice used for light-sheet microscopy and confocal histology.

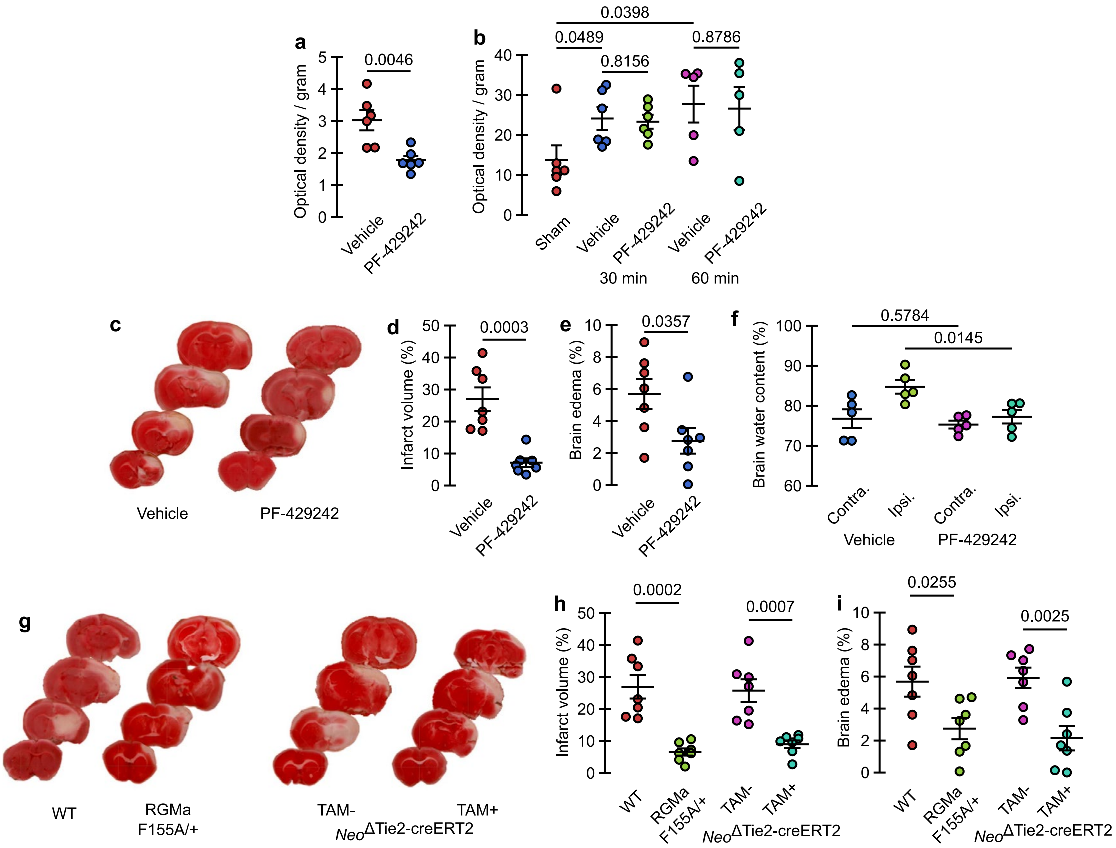

Extended Data Fig. 3 | Reduced ischemic brain injury after stroke in PF-429242 treated, RGMa-F155A/+ and *Neo*$^{\Delta Tie2\text{-}creERT2}$ mice. **a**, Optical density of Evans Blue dye per gram of retinal tissue 2 days after ocular ischemic insult in vehicle and PF-429242 treated mice. This suggests that PF-429242 treatment restores retinal blood barrier integrity (*n* = 6 retinas for each group). **b**, Optical density of Evans Blue dye per gram of liver tissue 2 days after liver ischemia (n = 6 for the sham group and both 30 min ischemia groups; n = 5 for both 60 min ischemia groups). **c**, Coronal brain slices stained with TTC showing the representative infarct area in vehicle and PF-429242 treated mice 7 days after MCAO. Infarcted metabolically inactive tissue appears white. **d-e**, Infract volume and brain edema relative to uninjured hemisphere for vehicle and PF-429242 treated mice (*n* = 7 for each group). **f**, Brain water content in MCAO and contralateral hemispheres in vehicle and PF-429242 treated mice (*n* = 5 for each group). **g**, Coronal brain slices stained with TTC showing the representative infarct area in WT, RGMa$^{F155A/+}$, and *Neo*$^{\Delta Tie2\text{-}creERT2}$ TAM + /- mice. Infarcted metabolically inactive tissue appears white. **h-i**, Infarct volume and brain edema relative to the uninjured hemisphere for control WT, RGMa$^{F155A/+}$, *Neo*$^{\Delta Tie2\text{-}creERT2}$ (TAM- or TAM +) mice (*n* = 7 for each group). All graphs indicate mean ± SEM. Each dot represents an independent experiment. Significance was assessed using two-tailed unpaired t-tests.

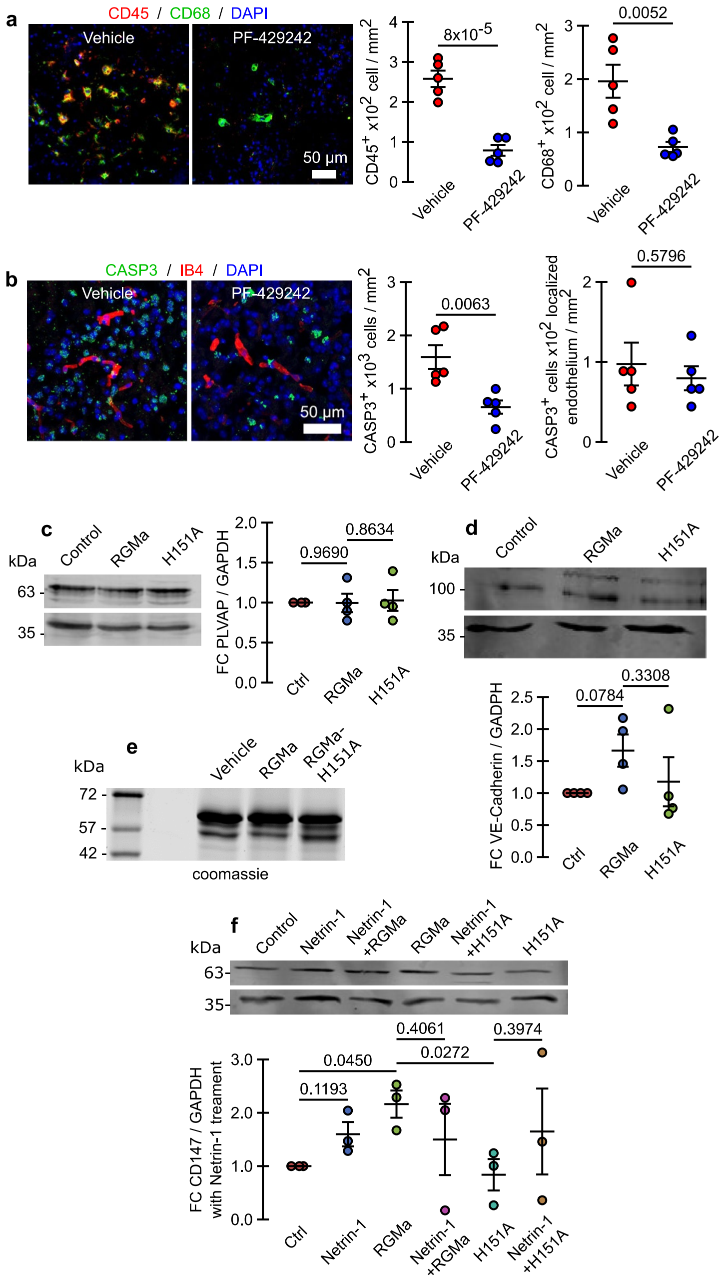

Extended Data Fig. 4 | Mechanistic studies of the role of RGMa cleavage. **a**, Staining for the immune cell markers CD45 and CD68 revel that treatment with PF-429242 reduces immune cell infiltrate in the peri-infarct area following MCAO ($n = 5$ brain per condition). **b**, Caspase-3 staining of the peri infarct region show that PF-429242 treatment significantly reduces the number of caspase-3 positive cells following MCAO. Co-localization of the endothelial cell marker IB4 and caspase 3 indicate that PF-429242 does not change the number of double positive cells following MCAO. **c**, bEnd.3 cells were treated RGMa and RGMa-H151A, and cell lysates were analyzed in Western Blotting. This shows that RGMa and RGMa-H151A do not affect the expression of PLVAP. **d**, bEnd.3 cells were treated RGMa and RGMa-H151A, and cell lysates were analyzed in Western Blotting. This shows that RGMa and RGMa-H151A do not affect the expression of VE-Cadherin. **e**, Coomassie stain of proteins in culture medium to confirm consistent protein loading for zymography for assay of relative activity of MMP2 and MMP9 in bEnd.3 cells cultured for 3 days with either vehicle, RGMa, or RGMa-H151A assessed with gelatin zymography. **f**, bEnd.3 cells were treated with Netrin and RGMa proteins before Western Blotting for CD147 was done. This shows that Netrin does not significantly alter the expression of CD147. All graphs are expressed as mean ± SEM. Each dot represents an independent experiment. Significance was assessed using two-tailed unpaired t-tests. When comparing to the normalizing control group a two-tailed one-sample t-test against a mean of one was used.

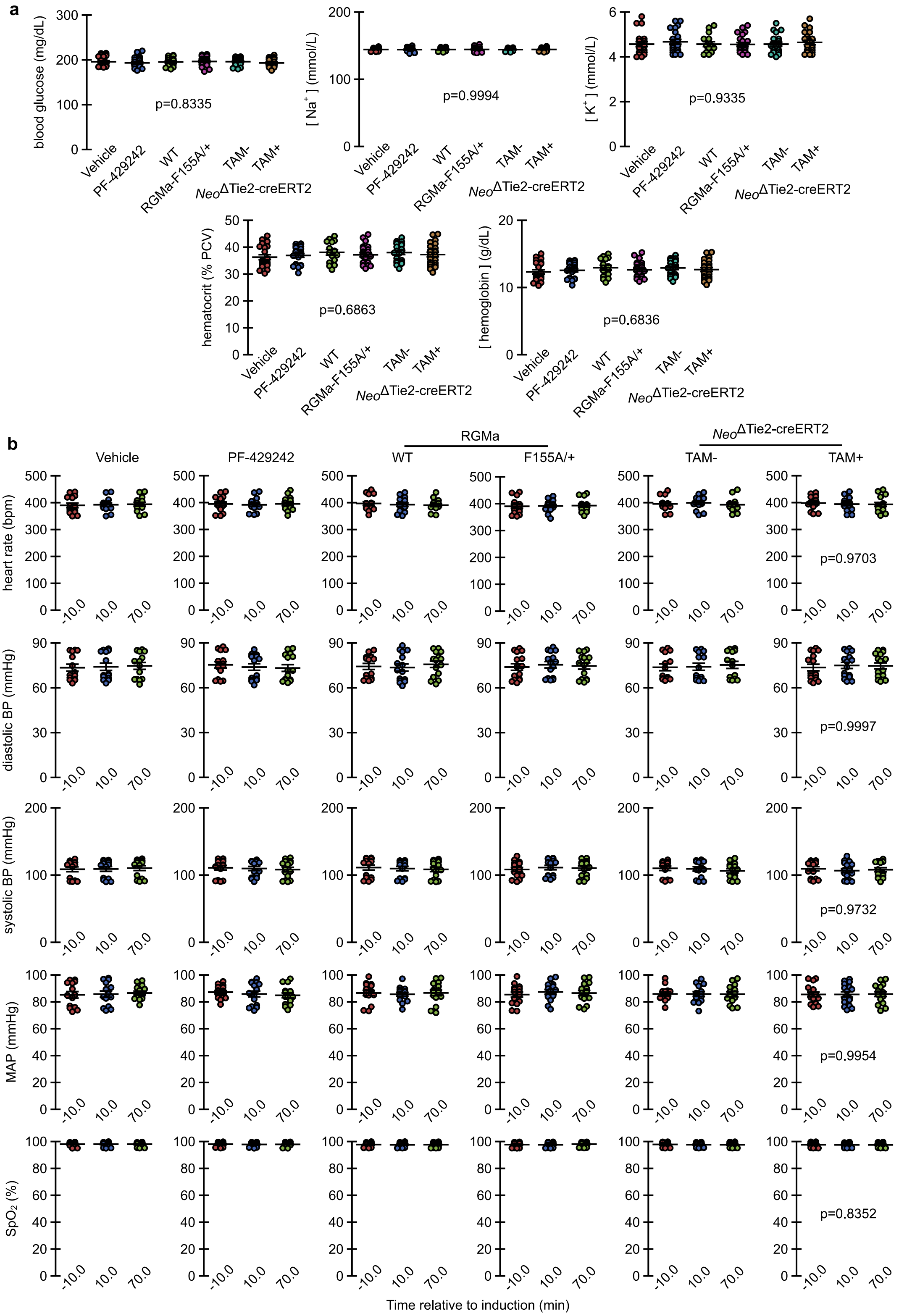

Extended Data Fig. 5 | Physiological monitoring of blood parameters in mice during MCAO for all experimental groups and their respective controls. **a**, Concentration of blood glucose, sodium, potassium, hematocrit (% packed cell volume (PCV)), and hemoglobin. **b**, Heart rate, systolic blood pressure, diastolic blood pressure, mean arterial pressure (MAP) and peripheral oxygen saturation (SpO$_2$). All graphs indicate mean ± SEM. Each dot represents an independent experiment and in panel **b** an independent experiment at one of three time-points. In panel **a**, group differences between each parameter were assessed with one-way ANOVAs (*P* values indicated). In panel **b**, group differences between each parameter were assessed with repeated-measures factorial ANOVAs (between-groups *P* values indicated).

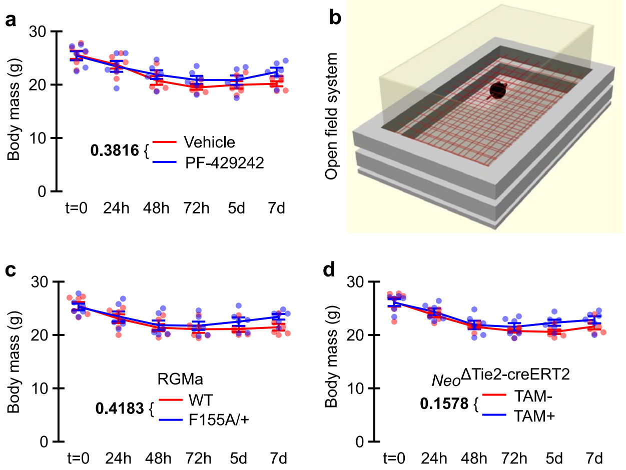

Extended Data Fig. 6 | Body weight of mice post-MCAO were comparable across treatment conditions. a, PF-429242 treated vs. vehicle. **b**, Schematic of Amonlite open field test system for mice. Mice were permitted to roam freely within the chamber for duration of 10 min. The chamber's inner dimensions are length 45 cm × width 24 cm × height 21 cm. The inferred laser beams used for movement detection are depicted as red (false color). The chamber ceiling is not shown. **c**, RGMa$^{F155A/+}$ vs. WT. **d**, *Neo*$^{\Delta Tie2\text{-}creERT}$ TAM+ vs. TAM-. All graphs indicate mean ± SEM. Each dot represents an independent experiment at a given time-point. Group differences were assessed with repeated-measures factorial ANOVAs (between-group *P* values in the legends).

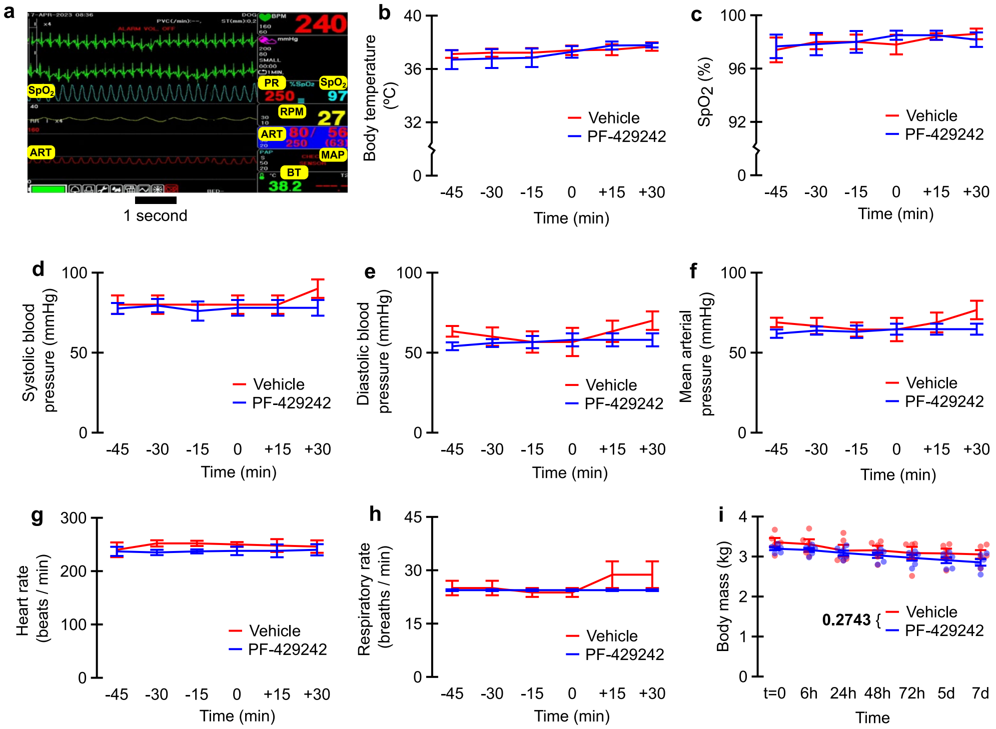

Extended Data Fig. 7 | Physiological parameters monitored before and after rabbit embolization. **a**, Physiological monitor readout. **b**-**h**, Parameters recorded during procedure relative to time of embolization. **b**, Body temperature (BT). **c**, Peripheral oxygen saturation (SpO_2). **d**-**f**, Intra-arterial blood pressure (ART): systolic blood pressure, diastolic blood pressure, and mean arterial pressure (MAP, computed), respectively. **g**, Heart/pulse rate (PR). **h**, Respiratory rate (RPM). **i**, Body mass evaluated until 7 days after embolization. All graphs indicate mean ± SEM. In panel **i**, each dot represents an independent experiment at a given time-point. Group differences were assessed with a repeated measures factorial ANOVA (between-group *P* value in the legend).

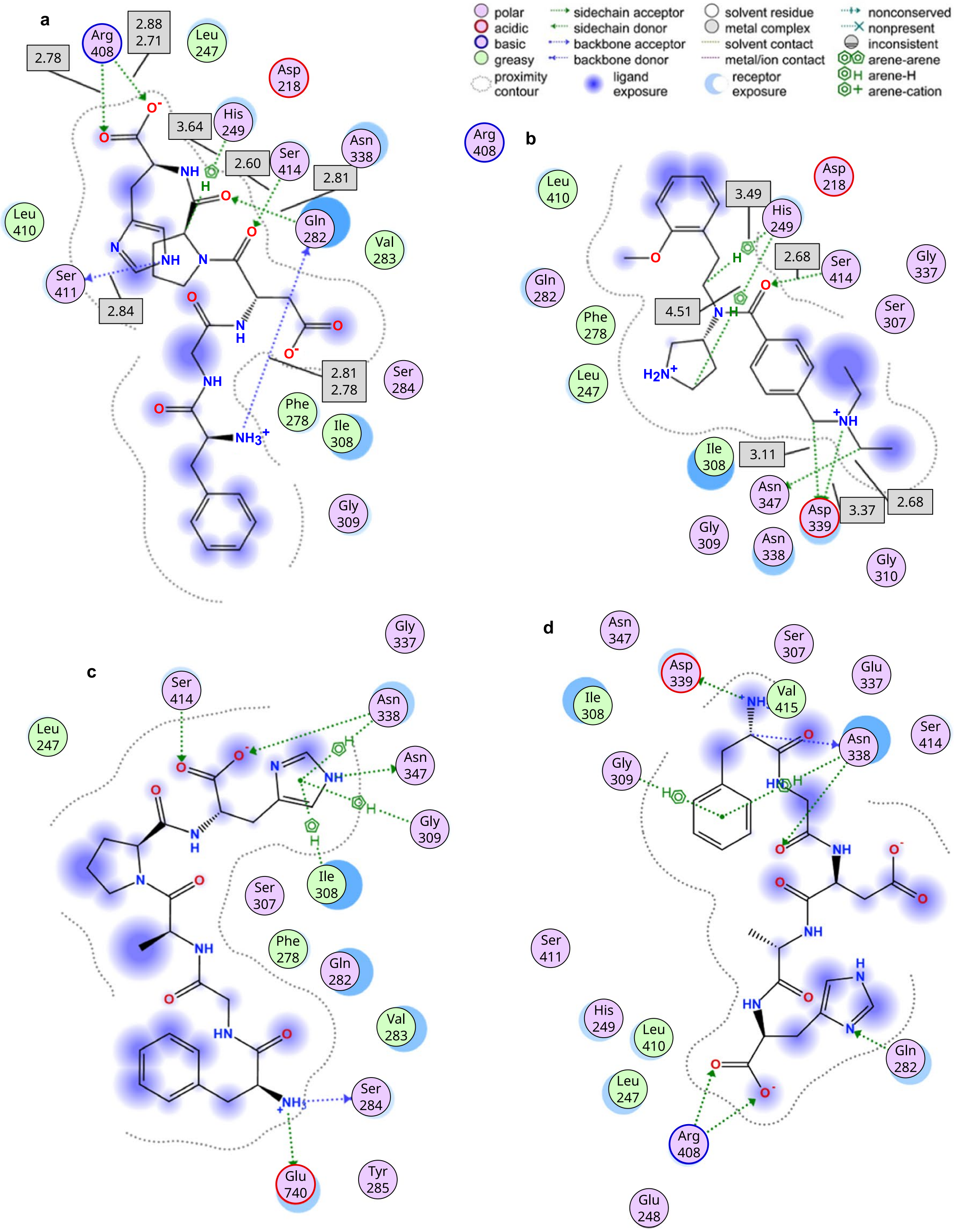

Extended Data Fig. 8 | Ligand interaction diagrams for SKI-1 active site. **a**, The ligand is the peptide sequence, FGDPH, on RGMa targeted by SKI-1. **b**, The ligand is the small molecule, PF-429242, shown to inhibit SKI-1 proteolytic activity. **c-d**, The ligands are mutant RGMa peptide sequences corresponding to the cleavage inhibiting mutations D149A and P150A, respectively. Ligand interactions with SKI-1 are shown with dotted lines and bond distance (in angstroms) are indicated in the grey boxes. PF-429242 shares several key binding interactions consistent with the RGMa target sequence, including H-bonding with the SKI-1 catalytic residue Ser414. Both mutant peptides fail to dock in an orientation that places catalytic residues proximal to the cleavage site, supporting the specificity of our modelling.

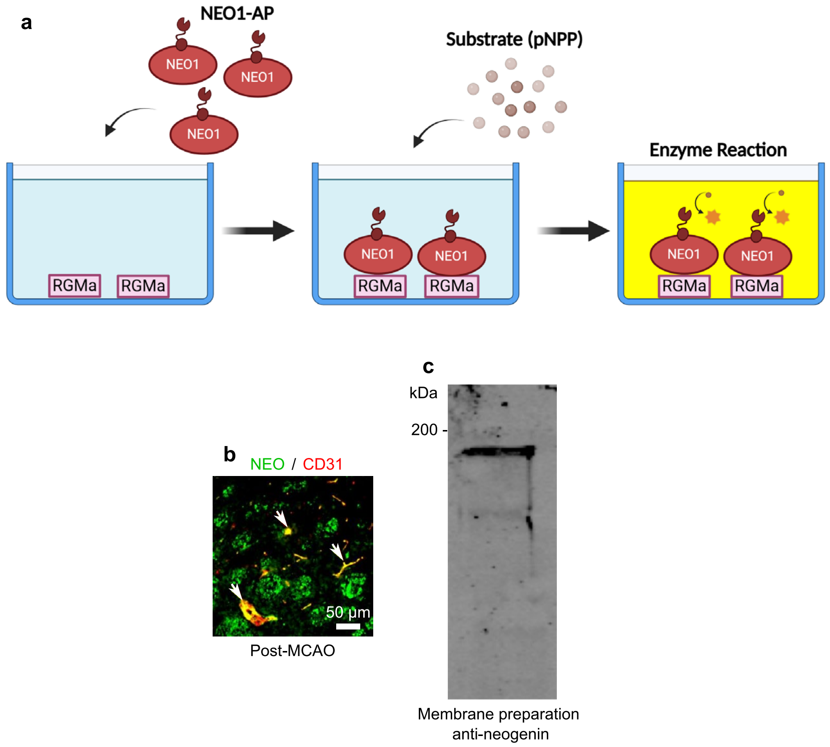

Extended Data Fig. 9 | Interaction assay. a, Interaction assay schematic. Plates were coated with RGMa. The interaction with Neogenin-AP, was revealed by a colorimetric reaction of AP (https://BioRender.com/kp25vlc). **b**, Neogenin co-localized with CD31-labled endothelial cells within the stroke penumbra in mice. White arrows indicate co-labeled endothelial cells. **c**, Membrane preparations of bEnd.3 cells were blotted and probed with anti-Neogenin, showing the expected ~200 kDa band.

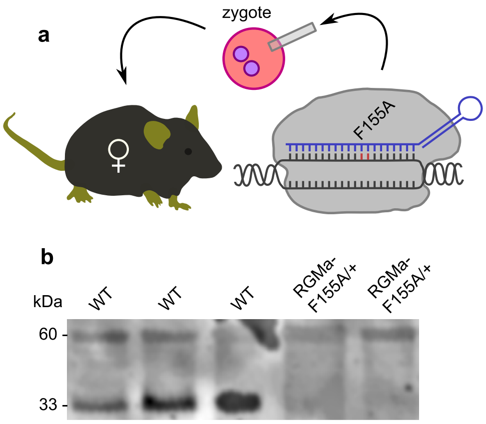

Extended Data Fig. 10 | Reduced RGMa cleavage in RGMa$^{F155A/+}$ mice brains. **a**, Schematic of generating the transgenic RGMa-F155A mouse line. **b**, Western blot performed on brain matrix extracts with anti-RGMa reveals a strong reduction in the cleaved form of RGMa in the brains of RGMa$^{F155A/+}$ point-mutant mice.

nature portfolio

Corresponding author(s): Philippe P. Monnier
Last updated by author(s): Feb 10, 2025

Reporting Summary

Nature Portfolio wishes to improve the reproducibility of the work that we publish. This form provides structure for consistency and transparency in reporting. For further information on Nature Portfolio policies, see our Editorial Policies and the Editorial Policy Checklist.

Statistics

For all statistical analyses, confirm that the following items are present in the figure legend, table legend, main text, or Methods section.

n/a	Confirmed	
☐	☒	The exact sample size (*n*) for each experimental group/condition, given as a discrete number and unit of measurement
☐	☒	A statement on whether measurements were taken from distinct samples or whether the same sample was measured repeatedly
☐	☒	The statistical test(s) used AND whether they are one- or two-sided *Only common tests should be described solely by name; describe more complex techniques in the Methods section.*
☐	☒	A description of all covariates tested
☐	☒	A description of any assumptions or corrections, such as tests of normality and adjustment for multiple comparisons
☐	☒	A full description of the statistical parameters including central tendency (e.g. means) or other basic estimates (e.g. regression coefficient) AND variation (e.g. standard deviation) or associated estimates of uncertainty (e.g. confidence intervals)
☐	☒	For null hypothesis testing, the test statistic (e.g. *F*, *t*, *r*) with confidence intervals, effect sizes, degrees of freedom and *P* value noted *Give P values as exact values whenever suitable.*
☒	☐	For Bayesian analysis, information on the choice of priors and Markov chain Monte Carlo settings
☒	☐	For hierarchical and complex designs, identification of the appropriate level for tests and full reporting of outcomes
☒	☐	Estimates of effect sizes (e.g. Cohen's *d*, Pearson's *r*), indicating how they were calculated

Our web collection on statistics for biologists contains articles on many of the points above.

Software and code

Policy information about availability of computer code

Data collection	LI-COR Odyssey, LaVision BioTec ImSpector Pro 5.1, Zen Microscopy 3.3, Amonlite 1.1, PeriSoft for Windows 2.5.5, OBS Studio 29.1.2, SMART Control 6.2, Syngo MR VE11C, FlowJo 10.0.6.
Data analysis	Prism GraphPad 9, ImageJ 1.53, Imaris 9.9, Eclipse 4.31 (JDK 21), Apache Commons Math 3.6, Inkscape 1.3 (for data presentation). All code used to generate the figures in this publication are available on GitHub (https://github.com/DeneRinguette/Shabanzadeh2025).

For manuscripts utilizing custom algorithms or software that are central to the research but not yet described in published literature, software must be made available to editors and reviewers. We strongly encourage code deposition in a community repository (e.g. GitHub). See the Nature Portfolio guidelines for submitting code & software for further information.

Data

Policy information about availability of data

All manuscripts must include a data availability statement. This statement should provide the following information, where applicable:

- Accession codes, unique identifiers, or web links for publicly available datasets
- A description of any restrictions on data availability
- For clinical datasets or third party data, please ensure that the statement adheres to our policy

All data generated and analyzed in this study is available on Zenodo (https://zenodo.org/records/15843737). The single-cell RNA sequencing (scRNA-seq) datasets generated and analyzed in this study are available in the Gene Expression Omnibus (GEO) under accession number GSE300442. Source data are provided with this paper.

Research involving human participants, their data, or biological material

Policy information about studies with human participants or human data. See also policy information about sex, gender (identity/presentation), and sexual orientation and race, ethnicity and racism.

Reporting on sex and gender	Biological sex was recorded by physicians during clinical data collection. Sex of subjects is reported in source data.
Reporting on race, ethnicity, or other socially relevant groupings	N/A
Population characteristics	Age, biological sex, and limited medical history which included hypertension, hyperlipidemia, diabetes mellitus, obesity, current smoking status, antiplatelet agents, and oral anticoagulants were reported.
Recruitment	This study was a matched subject, single-center prospective registered cohort trial with eligibility based on diffusion-weighted MRI and non-contrast head CT. A group of healthy controls who had no history of previous ischemic or other neurological disorders were recruited from the Physical Examination Center at the same hospital.
Ethics oversight	The First Affiliated Hospital of Chongqing Medical University Ethics Committee

Note that full information on the approval of the study protocol must also be provided in the manuscript.

Field-specific reporting

Please select the one below that is the best fit for your research. If you are not sure, read the appropriate sections before making your selection.

☒ Life sciences ☐ Behavioural & social sciences ☐ Ecological, evolutionary & environmental sciences

For a reference copy of the document with all sections, see nature.com/documents/nr-reporting-summary-flat.pdf

Life sciences study design

All studies must disclose on these points even when the disclosure is negative.

Sample size	Required sample sizes were estimated a priori using experiments believed to have similar estimated effect sizes. Formal a priori power analysis was not conducted.
Data exclusions	Data was only excluded when experimental error produced poor quality images which precluded accurate analysis.
Replication	Replication beyond the explicitly shown data was not conducted. The "n" in each figure presents the number of independent replicates.
Randomization	Mice were randomly chosen from litter mate pairs where applicable for group assignment. Genotype groups were assigned after experiments based on PCR identification. Drug treatment groups were designed before the animals were submitted to injections by a third person.
Blinding	Those collecting data were binded to group identity. Data collection and quantification were performed by different individuals. Analysis metadata (typically segmented regions) used for the quantification of acquired data was archived and independently inspected for quality. Genotype testing was done after experiments to ensure experimenter blinding.

Reporting for specific materials, systems and methods

We require information from authors about some types of materials, experimental systems and methods used in many studies. Here, indicate whether each material, system or method listed is relevant to your study. If you are not sure if a list item applies to your research, read the appropriate section before selecting a response.

Materials & experimental systems

n/a	Involved in the study	
☐	☒	Antibodies
☐	☒	Eukaryotic cell lines
☒	☐	Palaeontology and archaeology
☐	☒	Animals and other organisms
☐	☒	Clinical data
☒	☐	Dual use research of concern
☒	☐	Plants

Methods

n/a	Involved in the study	
☒	☐	ChIP-seq
☐	☒	Flow cytometry
☐	☒	MRI-based neuroimaging

Antibodies

Antibodies used

Primary antibody:
Transferrin Rabbit, monoclonal Abcam, ab214039
GAPDH Mouse, monoclonal Invitrogen, am4300
RGMa Goat, polyclonal Santa Cruz, Y-13
Neogenin Rabbit, polyclonal Santa Cruz, H-175
CD31 / Pecam1 Goat, polyclonal R&D, AF3628
BSG / CD147 Rabbit, monoclonal Invitrogen, MA5-32534
GFAP Rabbit, polyclonal Proteintech, 16825-1-AP
Isolectin-IB4, Griffonia simplicifolia Invitrogen, I21411
CXCL12 / SDF1-alpha Rabbit, polyclonal Abcam, ab25117
SKI-1 / Mbtps1 Rabbit, polyclonal LSBio, LS-C805152
Car4 / CA-IV Goat, polyclonal Invitrogen, PA5-47312
NeuN Rabbit, polyclonal Abcam, ab104225
NEFH Rabbit, polyclonal Sigma-Aldrich, N4142
6x-His Tag Mouse, monoclonal Invitrogen, MA1-21315
pFAK Rabbit, monoclonal Abcam, ab81298
FAK Mouse, monoclonal Invitrogen, AHO1272
PLVAP Rabbit, polyclonal Invitrogen, PA5-115774
CD147 Rabbit, monoclonal Invitrogen, MA5-32534
pVEGFR2 Rabbit, polyclonal Invitrogen, 44-1052
UNC5B (Neutralizing Antibody) Goat, polyclonal Bio-techne, AF1006
VE-Cadherin Rabbit, polyclonal Invitrogen, 36-1900
Caspase 3 Goat, polyclonal Invitrogen, PA5-142227
CD45 Rabbit, monoclonal Abcam, ab317446
CD68 Rat, monoclonal Invitrogen, MA5-16674
Desmin Rabbit, monoclonal Abcam, ab32362
Isolectin GS-IB4, Griffonia simplicifolia, I21412

Secondary antibody:
Donkey anti-rabbit IgG Alexa Fluor 488 Invitrogen, A-21206
Donkey anti-mouse IgG IRDye 800 CW Licor, 926-32212
Donkey anti-goat IgG Alexa Fluor 555 Invitrogen, A-21432
Donkey anti-rabbit IgG Alexa Fluor 568 Invitrogen, A-10042
Donkey anti-rabbit IgG IRDye 800CW Licor, 926-32213
Donkey anti-mouse IgG IRDye 680RD Licor, 926-68072
Goat anti-rat IgG Alexa Fluor 488 Invitrogen, A-11006
Donkey anti-goat IgG Alexa Fluor 488 Invitrogen, A-11055

Flow cytometry:
CD31/Pecam1 #12-0311-82, clone 390 BD Pharmingen
CD45 #17-0451-82, clone 30-F11 eBiosciences

Validation

Western blots were used to validate antibodies against their intended target proteins. Patterns obtained with the antibodies were compared to pattern provided by the manufacturer.

Eukaryotic cell lines

Policy information about cell lines and Sex and Gender in Research

Cell line source(s)	HEK-293 and CRL-2299 (bEnd.3) cells were obtained from ATCC.
Authentication	Both cell lines used were ordered directly from a trusted provider.
Mycoplasma contamination	Yes, tested with PCR. The cell lines tested negative for mycoplasma.
Commonly misidentified lines (See ICLAC register)	No commonly misidentified cell lines were used in the study.

Animals and other research organisms

Policy information about studies involving animals; ARRIVE guidelines recommended for reporting animal research, and Sex and Gender in Research

Laboratory animals	C57BL/6 mice, Sprague Dawley rats, and New Zealand white rabbits
Wild animals	No wild animals were used in this study.
Reporting on sex	Only male mice, rats, and rabbits were used as their respective stroke models have been shown to be more effective in producing consistent and reproducible results.
Field-collected samples	No field collected samples were used in the study.
Ethics oversight	Animal Care Committee (University Health Network)

Note that full information on the approval of the study protocol must also be provided in the manuscript.

Clinical data

Policy information about clinical studies

All manuscripts should comply with the ICMJE guidelines for publication of clinical research and a completed CONSORT checklist must be included with all submissions.

Clinical trial registration	ChiCTR1800018569
Study protocol	Supplementary information
Data collection	The study participants consisted of patients with acute ischemic stroke (AIS) who were admitted to the neurological department of our university hospital (the First Affiliated Hospital of Chongqing Medical University) within 24 hours after stroke onset or first found abnormal (FFA). Patients were recruited in the study if they were ≥ 18 years old with ischemic stroke which was confirmed by diffusion-weighted MRI. The exclusive criteria consisted of intracranial hemorrhage on non-contrast cranial CT (NCCT) at admission, transient ischemic stroke, malignant tumors, renal failure, hepatic disease, autoimmune disease, acute or chronic infections, inflammatory diseases, alcohol abuse, drug abuse, or any severe systemic diseases. All MRIs and CTs were read by an independent committee. During the same period, a group of healthy controls who had no history of previous ischemic or other neurological disorders were recruited from the Physical Examination Center at the same hospital. Healthy subjects were matched with patients in terms of age and sex composition. Blood sample collection was carried out in accordance with sterile requirements.
Outcomes	N/A

Plants

Seed stocks	N/A.
Novel plant genotypes	N/A.
Authentication	N/A.

Flow Cytometry

Plots

Confirm that:

☒ The axis labels state the marker and fluorochrome used (e.g. CD4-FITC).

☒ The axis scales are clearly visible. Include numbers along axes only for bottom left plot of group (a 'group' is an analysis of identical markers).

☐ All plots are contour plots with outliers or pseudocolor plots.

☒ A numerical value for number of cells or percentage (with statistics) is provided.

Methodology

Sample preparation	Mice were euthanized by cervical dislocation under isoflurane anesthesia. The mouse brains were dissected out of the skulls and divided into hemispheres. They were then quickly minced in a petri dish on ice, using two surgical blades. For FACS sorting, a cell suspension was obtained upon digesting the tissue in 2 mg/ml Dispase II (D4693, Sigma-Aldrich, Steinheim, Germany), 2 mg/mL Collagenase IV (#1710401, Thermo Fisher Scientific, Zurich, Switzerland) and 2 mM CaCl2 PBS solution for 40 min at 37°C with occasional shaking. The suspension was filtered sequentially through 100/70/40 µm cell strainers (#431751, Corning, New York, USA) to remove large cell debris. Cells were then centrifuged 700 RCF for 7 min at 4°C. In case a visible myelin pellet was observed, 5 mL 25% BSA (ice cold) was overlaiyed with 5 mL of the sample, centrifuged at 2200 RCF for 22 min (4°C). The supernatant was removed (including the lipid phase) and the pellet was resuspended in 9 ml PBS, followed by another round of centrifugation at 700 RCF for 7 min (4°C). Supernatant was subsequently discarded, while the cell pellets were resuspended in 3 mL of ACK hemolytic buffer at room temperature for 3 minutes. To stop the reaction, 30 mL of ice-cold PBS was added to the mixture and centrifuged at 700 RCF for 7 min at 4°C. The cell pellets were resuspended in FACS buffer (PBS + 1% BSA). For FACS sorting, the cells were stained with anti- CD31 PE conjugated antibody in a concentration of 1:20 (#12-0311-82, clone 390, BD Pharmingen) and anti-CD45 APC conjugated antibody in a concentration of 1:20 (#17-0451-82, clone 30-F11, eBiosciences) for 45 min at 4° C, protected from light. Thereafter, the cells were washed with 1 mL of FACS buffer, centrifuged in a tabletop centrifuge at 700 RCF at 4°C for 7 min. Finally, the cell pellets were resuspended in appropriate volumes of FACS buffer (PBS + 1% Bovine Serum Albumin) and the suspension was passed through a 35 µm cell strainer of a FACS sorting tube (#352235, Corning).
Instrument	Cells were sorted by a FACS Aria III (648282D2, BD Bioscience) sorter using the four-way purity sorting mode directly in FACS buffer.
Software	Live events were acquired and analyzed using Flowjo software (Tree Star Inc.).
Cell population abundance	Cell abundance was determined by final population of interest (cd31+/cd45-) divided by all intact cell counts. Final populations of less than 7000 cells were not used for subsequent scRNA-seq analysis. Trypan dye was used to assess post-sort sample viability, a sample less than 90% would be rejected.
Gating strategy	FSC-A/SSC-A : 40K-250K / 0K-170K, subsequent gating graphically represented in Extended Data Figure 1.

☒ Tick this box to confirm that a figure exemplifying the gating strategy is provided in the Supplementary Information.

Magnetic resonance imaging

Experimental design

Design type	Resting state; event-related.
Design specifications	Single imaging session to assess contrast agent leakage into brain.
Behavioral performance measures	Behavioral testing not done during MRI.

Acquisition

Imaging type(s)	DWI and DCE
Field strength	1.5 T
Sequence & imaging parameters	Imaging included anatomical T2-weighted FLAIR imaging (SPACE, 0.8 × 0.8 × 1 mm resolution), diffusion-weighted imaging (DWI) for infarct quantification (RESOLVE DW-EPI, 0.8 × 0.8 × 2 mm resolution; b-values 0 s/mm2 and 1000 s/mm2), and pre-contrast T1 mapping (3D-VIBE, variable flip angle technique; 0.8 × 0.8 × 2 mm resolution; 2°, 9°, and 19° flip angles) combined with dynamic contrast-enhanced imaging for vascular leakage assessment (3D-VIBE; 0.8 × 0.8 × 2 mm resolution; 20° flip angle; 144 repetitions; 3.9 sec temporal resolution, 4.63 ms repetition time (TR), 1.87 ms time to echo (TE)), with full brain coverage in the axial plane and consistent imaging field-of-views (15.7 × 15.7 cm) for all acquisitions to facilitate image registration.
Area of acquisition	Full brain in axial plane

Diffusion MRI ☒ Used ☐ Not used

Parameters: b-values 0 s/mm2 and 1000 s/mm2

Preprocessing

Preprocessing software	N/A
Normalization	Data was not normalize as linear scale is irrelevant to our parameter modeling.

Normalization template	Data was not normalize.
Noise and artifact removal	N/A
Volume censoring	N/A

Statistical modeling & inference

Model type and settings	N/A
Effect(s) tested	Two-sample two-tailed t-test of infract volume (DWI) and Relative Delta K-trans (DCE, Patlak model)

Specify type of analysis: ☒ Whole brain ☐ ROI-based ☐ Both

Statistic type for inference (See Eklund et al. 2016)	Voxel-wise
Correction	N/A

Models & analysis

n/a | Involved in the study
- ☒ ☐ Functional and/or effective connectivity
- ☒ ☐ Graph analysis
- ☐ ☒ Multivariate modeling or predictive analysis

Multivariate modeling and predictive analysis	N/A